Bar-induced Perturbation Strengths of the Galaxies in the Ohio State University Bright Galaxy Survey – I

E. Laurikainen – University of Oulu, Finland

H. Salo – University of Oulu, Finland

R. Buta – University of Alabama

S. Vasylyev – University of Alabama

Citation of published version:

Laurikainen, E., Salo, H., Buta, R., Vasylyev, S. (2004): Bar-induced Perturbation Strengths of the Galaxies in the Ohio State University Bright Galaxy Survey – I. *Monthly Notices of the Royal Astronomical Society,* 355(4).
DOI: https://doi.org/10.1111/j.1365-2966.2004.08410.x

Mon. Not. R. Astron. Soc. **355,** 1251–1271 (2004) doi:10.1111/j.1365-2966.2004.08410.x

Bar-induced perturbation strengths of the galaxies in the Ohio State University Bright Galaxy Survey – I

Eija Laurikainen,[1]★ Heikki Salo,[1] Ronald Buta[2] and Sergiy Vasylyev[2]

[1]*Division of Astronomy, Department of Physical Sciences, PO Box 3000, University of Oulu, Oulu, FIN-90014, Finland*
[2]*Department of Physics and Astronomy, Box 870324, University of Alabama, Tuscaloosa, AL 35487, USA*

Accepted 2004 September 10. Received 2004 September 10; in original form 2004 June 4

ABSTRACT

Bar-induced perturbation strengths are calculated for a well-defined magnitude-limited sample of 180 spiral galaxies, based on the Ohio State University Bright Galaxy Survey. We use a gravitational torque method, the ratio of the maximal tangential force to the mean axisymmetric radial force, as a quantitative measure of the bar strength. The gravitational potential is inferred from an H-band light distribution by assuming that the M/L ratio is constant throughout the disc. Galaxies are deprojected using orientation parameters based on B-band images. In order to eliminate artificial stretching of the bulge, two-dimensional bar–bulge–disc decomposition has been used to derive a reliable bulge model. This bulge model is subtracted from an image, the disc is deprojected assuming it is thin, and then the bulge is added back by assuming that its mass distribution is spherically symmetric. We find that removing the artificial bulge stretch is important especially for galaxies having bars inside large bulges. We also find that the masses of the bulges can be significantly overestimated if bars are not taken into account in the decomposition.

Bars are identified using Fourier methods by requiring that the phases of the main modes ($m = 2$, $m = 4$) are maintained nearly constant in the bar region. With such methods, bars are found in 65 per cent of the galaxies in our sample, most of them being classified as SB-type systems in the near-infrared by Eskridge and co-workers. We also suggest that as much as $\approx$70 per cent of the galaxies classified as SAB-types in the near-infrared might actually be non-barred systems, many of them having central ovals. It is also possible that a small fraction of the SAB-type galaxies have weak non-classical bars with spiral-like morphologies.

Key words: galaxies: spiral – galaxies: statistics.

1 INTRODUCTION

In two previous papers (Buta, Laurikainen & Salo 2004, hereafter BLS; Laurikainen, Salo & Buta 2004, hereafter LSB), we have used a gravitational torque parameter to investigate two issues: the distribution of maximum relative bar torques in spiral galaxies, and the impact of bar strength on nuclear activity type in the same galaxies. These studies have utilized a detailed analysis of 158 galaxies from the Ohio State University Bright Galaxy Survey (OSUBGS; Eskridge et al. 2002, hereafter EFP) and 22 galaxies from the Two-Micron All-Sky Survey (2MASS; Skrutskie et al. 1997). In the present paper, we present the full details of our methods used to derive maximum relative gravitational torques for bars and, in some cases, spirals. Our method is a refinement of the approach used by Buta & Block (2001, hereafter BB) to derive quantitative bar strengths from near-infrared (near-IR) images.

2 SAMPLE AND DATA REDUCTIONS

The OSUBGS forms a sample of 205 nearby spiral galaxies, originally selected to fill the following criteria: type index in the Third Reference Catalogue of Bright Galaxies (de Vaucouleurs et al. 1991, hereafter RC3) $0 < T < 9$ (S0/a to Sm), total magnitudes $B_T < 12.0$, standard isophotal galaxy diameters $D_{25} < 6.5$ arcmin, and declinations in the range $-80^\circ < \delta < +50^\circ$. In this paper, only OSUBGS galaxies with inclinations less than 65° are included, which limited the sample to 158 galaxies. This corresponds approximately to RC3 standard isophotal axial ratio $\log R_{25} \leqslant 0.38$. The 22 2MASS galaxies satisfy the same criteria as the galaxies in the OSUBGS, except that they have $D_{25} > 6.5$ arcmin. The final sample of 180 galaxies is representative of typical luminous spiral galaxies in the nearby Universe. It was shown by BLS that the sample is

★E-mail: eija.laurikainen@oulu.fi

biased mainly against late-type, low-luminosity barred spirals, based on a comparison to a distance-limited sample of 1264 galaxies from the catalogue of Tully (1988).

We use the *B*- and *H*-band images of the OSUBGS sample, available as an early release by EFP.[1] The *B*-band images reach typically the surface brightnesses of 26 mag arcsec^{-2}, whereas the limiting surface brightness in the *H* band is typically 20 mag arcsec^{-2} (EFP). Our reduction steps consist of cleaning the images of bad pixels and foreground stars, background subtraction, and for some of the galaxies also removal of background gradients. We also checked the image scales and orientations of the *B*-band images using the *H*-band images as a frame of reference. This is important, because the orientation parameters are measured in the *B* band, which are then used to deproject the *H*-band images to face-on orientation.

The pixel sizes were checked using the IRAF routine GEOMAP: the *H*-band images were used as reference frames and magnification factors were calculated for the *B*-band images. Generally, the same pixel sizes were obtained that were listed in the image headers of the *B*-band images; however, for 17 of the galaxies the header value was too small by a factor of 2 (0.36 arcsec instead of 0.72 arcsec). All of these galaxies were observed using the same telescope, the Perkins 1.8-m reflector, and the same instrument, a Low NSF T1800 CCD, in the *B* band. In the *H* band, the 1.8-m Perkins reflector was also used, but with the OSIRIS instrument attached. As the same instrumentation was used also for 66 other galaxies, which had no inconsistencies in the pixel sizes between the *B*- and *H*-band images, we conclude that there must be an error in the *B*-band image headers of the 17 discrepant galaxies. The corrected pixel sizes are denoted by footnotes in Table 1. In the 2MASS sample, the scale of the *H*-band images is 1.0 arcsec pixel^{-1}.

The IRAF routine GEOMAP was used also to check the relative differences in the direction of north in the sky plane between the *B*- and *H*-band images. The list of star positions for GEOMAP was produced by a semi-automatic IDL routine. Before applying GEOMAP, the *B*- and *H*-band images were transposed to have the same orientations in the sky. The shifts in the position angles between the two bands were found to be 4.°4 at maximum (dϕ in Table 1). In order to have the correct position angle in the *H*-band image, the shift given in the table must be added to the position angle of the *B*-band image.

Some of the images include large numbers of foreground stars so that point spread function (PSF) fitting had to be used to automatically remove the stars. Stars were identified with IRAF routine DAOFIND using the typical PSF FWHM in each image. IRAF routines PSF and ALLSTAR were used to subtract stars. In some cases, the model PSF was not good enough to remove all the stellar flux, probably because it was not exactly the same for faint and bright stars, or because the PSF varied in different parts of the image. In that case, cleaning was completed manually using the IRAF routine IMEDIT, which replaced the residual in an aperture by a two-dimensional (2D) polynomial fit interpolated from pixels in the surrounding annulus. The sky-background in the *H*-band images was already subtracted by EFP while combining the images, but the subtraction was fine-tuned by us, based on the mean values of the sky measured in different image positions. The sky gradients were generally small, but for some of the images IMSURFIT was applied to calculate linear polynomial fits in the *x*- or *y*-directions of the images.

The 2MASS images have approximately the same spatial resolution as the OSUBGS images, but they are not as deep. Also, the field of view was generally rather small so that mosaics of five or more images were typically constructed. Before combining the images, the overscan regions were removed and the background values given in the image headers were subtracted. Because the background levels varied in different parts of the images, the subtraction was fine-tuned, paying attention only to the background near to the galaxy. Positioning of the frames was carried out, using stars common in the image fields. Finally, the mosaics were cleaned of foreground stars and bad pixels.

[1] See http://www.astronomy.ohio-state.edu/~survey/EDR/index.html.

3 ORIENTATION PARAMETERS

Well-defined orientation parameters are important for the measurements of the perturbation strengths; it has been shown by BB and Laurikainen & Salo (2002, hereafter LS) that already uncertainties of 10 per cent in inclination can cause uncertainties of 10–15 per cent in the perturbation strength. All of our sample galaxies have orientation parameters listed in RC3. However, the OSU *B*-band images have sufficient field of view, and are of sufficient depth and quality compared to what was used for RC3, that they can be used to improve the orientation parameters in each case. They are also deeper than the OSU *H*-band images. The radial profiles of the major-axis position angles (ϕ) and minor-to-major axial ratios of the discs ($q = b/a$) were calculated using the ELLIPSE routine in IRAF. A linear radial scaling was used, and for the upper and lower deviant pixels a 3σ clipping criterion was applied. The position angles and corresponding axial ratios are listed in Table 1; these are means over the regions indicated in the table, and represent the outer parts of the discs rather than a specific isophotal level (as in RC3). For each parameter, the errors are standard deviations of the mean. For comparison, the orientation parameters (at $\mu_B = 25.00$ mag arcsec^{-2}) of the same galaxies from RC3 are also listed.

A few of the galaxies are in pairs, so that the outer parts of the discs are partially superimposed by the neighbouring galaxies. For these galaxies, masks were first created for the overlapping regions and then ellipse fits were performed on the unmasked parts of the images. Finally, the masked areas were replaced by the mean in an annulus at each radius covering the unmasked part of the annulus. For NGC 1808, the outer disc was so faint that the ellipse fitting failed for a large part of the disc, and the orientation parameters were obtained by fitting an ellipse to the shape of the outer pseudo-ring. Because only a narrow zone could be used for the fit, the errors in the orientation parameters are those given by the ellipse fitting routine. For NGC 1300, an automatic fit to the outer ring failed and the position angle and inclination were estimated manually. For the galaxies NGC 289 and 3893, the image field was slightly too small for reliable measurements, but even so the values we obtain are similar to those given in RC3. In any case, we used the RC3 orientation parameters for these galaxies. For three of the galaxies, NGC 278, 4138 and 5248, we had no *B*-band image so that the orientation parameters were determined using the *H*-band images. Comparison to the Digitized Sky Survey image showed that they were deep enough for that purpose. The galaxies NGC 2139 and 4496A are possible mergers, and therefore the uncertainty in their orientation parameters is large. For the galaxies in the 2MASS sample, we used mainly the orientation parameters as given in RC3, because the images were not very deep.

In Fig. 1 we compare our measured orientation parameters, axial ratio q and major axis position angle ϕ, with values from RC3 and from García-Gómez et al. (2004), who used the OSUBGS images to derive orientation parameters for most of the same galaxies using Fourier techniques. We make the comparisons by plotting the differences, $|\Delta q|$ and $|\Delta \phi|$, versus the means of q and ϕ for each pair

Table 1. Orientation parameters.

Galaxy	$q \pm sd$ (B)	$\phi \pm sd$	Range (arcsec)	q (RC3)	ϕ (RC3)	dϕ
OSUBGS						
ESO 138	0.708 ± 0.015	62.4 ± 3.7	420–460	0.72	55	−0.22
IC 4444[e]	0.826 ± 0.018	74.6 ± 1.9	120–140	0.83	–	+3.66
IC 5325	0.837 ± 0.006	27.5 ± 2.2	210–250	0.91	–	0.00
NGC 0150	0.498 ± 0.009	107.6 ± 2.7	260–320	0.48	118	+0.13
NGC 0157	0.724 ± 0.008	36.5 ± 1.2	180–210	0.65	40	+1.44
NGC 0210	0.654 ± 0.009	163.2 ± 1.5	275–310	0.66	160	−0.54
NGC 0278[d]	0.927 ± 0.005	65.8 ± 3.6	39–44	0.95	–	
NGC 0289[c]	0.789 ± 0.014	141.5 ± 2.5	400–420	0.71	130	0.00
NGC 0428	0.750 ± 0.013	100.5 ± 1.8	230–245	0.76	120	+1.54
NGC 0488	0.770 ± 0.010	5.6 ± 1.9	260–300	0.74	15	+1.95
NGC 0578	0.589 ± 0.014	101.7 ± 1.5	345–375	0.63	110	0.00
NGC 0613	0.772 ± 0.008	121.6 ± 1.5	360–430	0.76	120	−2.09
NGC 0685	0.787 ± 0.019	104.3 ± 3.7	320–345	0.89	–	+0.60
NGC 0864	0.842 ± 0.008	28.7 ± 4.7	160–172	0.76	20	−0.05
NGC 0908	0.456 ± 0.008	72.4 ± 0.3	440–460	0.44	75	+0.12
NGC 1042	0.781 ± 0.013	4.5 ± 1.9	300–330	0.78	15	+1.57
NGC 1058	0.877 ± 0.016	23.3: ± 3.3	190–200	0.93	–	+1.52
NGC 1073	0.875 ± 0.013	1.0 ± 4.2	250–280	0.91	15	+1.59
NGC 1084	0.753 ± 0.021	57.2 ± 1.1	210–230	0.56	115	−0.07
NGC 1087	0.609 ± 0.012	2.8 ± 0.1	190–210	0.60	5	0.00
NGC 1187	0.780 ± 0.019	132.0 ± 5.1	330–400	0.74	130	+0.20
NGC 1241	0.575 ± 0.011	147.5 ± 1.4	145–160	0.60	145	−0.17
NGC 1300[a]	0.760	150.0	355	0.66	106	−2.18
NGC 1302	0.941 ± 0.012	179.0: ± 4.3	280–310	0.95	–	−0.08
NGC 1309	0.926 ± 0.023	65.3 ±10.2	170–190	0.93	45	+0.27
NGC 1317	0.893 ± 0.013	64.5 ± 3.5	185–215	0.87	78	−0.07
NGC 1350	0.516 ± 0.004	4.1 ± 0.4	430–500	0.54	0	−2.25
NGC 1371	0.770 ± 0.009	127.6 ± 2.7	350–385	0.69	135	+0.30
NGC 1385	0.626 ± 0.011	171.9 ± 2.1	260–300	0.59	165	+0.25
NGC 1493	0.924 ± 0.022	51.3: ± 6.7	300–340	0.93	–	−0.09
NGC 1559	0.559 ± 0.009	63.2 ± 0.8	300–320	0.57	64	+0.20
NGC 1617	0.489 ± 0.004	111.5 ± 0.4	280–340	0.49	107	–
NGC 1637	0.823 ± 0.006	34.6 ± 1.6	200–230	0.81	15	+1.67
NGC 1703	0.869 ± 0.019	165.1 ± 9.5	150–180	0.89	–	+3.48
NGC 1792	0.453 ± 0.003	136.9 ± 0.1	300–330	0.50	137	−0.44
NGC 1808[b]	0.744 ± 0.013	119.5 ± 1.5	570	0.60	133	+1.38
NGC 1832	0.702 ± 0.023	11.0 ± 3.4	140–160	0.66	10	+0.41
NGC 2090	0.465 ± 0.000	18.1 ± 1.5	380–470	0.49	13	−0.36
NGC 2139	0.859 ± 0.024	121.6 ± 8.3	140–180	0.74	140	+3.56
NGC 2196	0.788 ± 0.018	44.3 ± 2.2	170–200	0.78	35	+3.54
NGC 2207	0.716 ± 0.017	136.9 ± 1.5	285–300	0.65	141	−0.36
NGC 2442	0.925 ± 0.009	110.7 ± 3.4	380–410	0.89	–	−0.37
NGC 2559	0.527 ± 0.005	2.1 ± 0.4	230–260	0.46	6	+3.46
NGC 2566	0.734 ± 0.018	115.8 ± 2.9	345–390	0.68	110	+3.57
NGC 2775	0.801 ± 0.009	163.5 ± 1.8	210–280	0.78	155	+2.95
NGC 2964	0.566 ± 0.004	96.8 ± 0.4	160–180	0.55	97	+1.45
NGC 3059	0.920 ± 0.022	3.3: ± 8.6	245–280	0.89	–	+3.37
NGC 3166	0.586 ± 0.013	82.5 ± 1.2	380–400	0.49	87	+1.66
NGC 3169	0.776 ± 0.020	56.4 ± 2.7	370–400	0.63	45	+1.64
NGC 3223	0.691 ± 0.018	125.0 ± 1.3	240–260	0.60	135	+3.53
NGC 3227	0.661 ± 0.013	153.1 ± 1.0	155–170	0.67	155	+1.96
NGC 3261	0.732 ± 0.024	71.0 ± 2.9	160–240	0.76	85	+3.47
NGC 3275	0.936 ± 0.017	152.6 ± 5.7	125–155	0.76	–	+3.49
NGC 3319	0.554 ± 0.012	32.8 ± 1.4	380–400	0.55	37	+4.36
NGC 3338	0.495 ± 0.008	93.6 ± 1.3	230–280	0.62	100	+4.36
NGC 3423	0.769 ± 0.012	31.2 ± 1.1	260–280	0.85	10	+3.67
NGC 3504	0.980 ± 0.012	–	145–170	0.78	–	1.32
NGC 3507	0.944 ± 0.056	91.9 ± 0.9	160–180	0.85	110	+1.43
NGC 3513	0.768 ± 0.016	75.4 ± 12.0	240–260	0.79	75	+3.51

Table 1 – *continued*

Galaxy	$q \pm sd$ (B)	$\phi \pm sd$	Range (arcsec)	q (RC3)	ϕ (RC3)	dϕ
NGC 3583	0.744 ± 0.019	119.2 ± 2.3	155–170	0.65	125	+2.35
NGC 3593	0.486 ± 0.021	86.2 ± 0.8	300–340	0.37	92	+4.27
NGC 3596[f]	0.829 ± 0.006	92.5 ± 5.3	235–260	0.95	–	+1.45
NGC 3646	0.599 ± 0.010	50.4 ± 1.3	320–350	0.58	50	+0.53
NGC 3675	0.494 ± 0.003	178.1 ± 0.3	240–270	0.52	178	+2.54
NGC 3681	0.901 ± 0.017	34.9 ± 5.7	140–150	0.79	–	+2.53
NGC 3684	0.704 ± 0.008	119.1 ± 1.0	185–200	0.69	130	+1.47
NGC 3686	0.753 ± 0.008	18.2 ± 1.0	150–190	0.78	15	+1.31
NGC 3726	0.624 ± 0.011	15.6 ± 0.0	340–350	0.69	10	+4.39
NGC 3810	0.680 ± 0.007	21.4 ± 1.1	260–300	0.71	15	+1.71
NGC 3887	0.710 ± 0.012	4.6 ± 1.1	240–260	0.76	20	+3.50
NGC 3893[c]	0.595 ± 0.010	170.1 ± 0.3	247–260	0.62	165	+1.77
NGC 3938	0.914 ± 0.020	37.2 ± 0.8	300–320	0.91	–	+1.90
NGC 3949	0.904 ± 0.020	103.4 ± 9.6	184–200	0.57	120	+4.35
NGC 4027	0.753 ± 0.009	163.1 ± 1.2	200–240	0.76	167	+3.43
NGC 4030	0.729 ± 0.009	26.7 ± 3.1	260–300	0.72	27	+3.47
NGC 4051	0.846 ± 0.154	128.0 ± 1.3	300–340	0.74	135	+0.69
NGC 4123[f]	0.677 ± 0.017	125.7 ± 1.4	270–320	0.74	135	0.00
NGC 4136[f]	0.958 ± 0.015	–	290–320	0.93	–	+0.71
NGC 4138[d]	0.598 ± 0.006	148.2 ± 0.7	50–62	0.66	150	
NGC 4145	0.572 ± 0.007	101.5 ± 0.5	380–410	0.72	100	+0.59
NGC 4151[a]	0.92	–	400	0.71	50	+0.73
NGC 4212[f]	0.663 ± 0.017	75.7 ± 0.8	220–260	0.62	75	+0.60
NGC 4242	0.672 ± 0.012	28.3 ± 1.8	250–310	0.75	25	+4.38
NGC 4254	0.868 ± 0.012	57.4 ± 5.6	380–400	0.87	–	+2.03
NGC 4293	0.463 ± 0.007	65.1 ± 0.4	310–390	0.46	72	+0.73
NGC 4303	0.861 ± 0.011	146.9 ± 1.8	390–440	0.89	–	+0.73
NGC 4314	0.959 ± 0.019	61.8 ± 15.1	240–280	0.89	–	+1.90
NGC 4394	0.902 ± 0.009	103.0 ± 3.7	185–210	0.89	–	+1.47
NGC 4414[f]	0.644 ± 0.011	160.0 ± 0.9	290–320	0.56	155	+0.33
NGC 4450	0.720 ± 0.009	2.2 ± 3.0	360–420	0.74	175	+0.64
NGC 4457[f]	0.883 ± 0.017	80.8 ± 2.1	230–250	0.85	–	+0.53
NGC 4487	0.659 ± 0.008	73.8 ± 0.8	290–340	0.68	100	+3.60
NGC 4490	0.441 ± 0.004	123.5 ± 0.5	320–380	0.49	125	+0.66
NGC 4496A[f]	0.788 ± 0.011	71.7 ± 1.6	280–300	0.47	–	+0.52
NGC 4504	0.631 ± 0.025	142.5 ± 3.4	200–330	0.62	30	+3.50
NGC 4527	0.456 ± 0.007	67.1 ± 0.6	420–440	0.34	67	+0.68
NGC 4548	0.744 ± 0.009	153.2 ± 1.7	315–350	0.79	150	+3.87
NGC 4571[f]	0.821 ± 0.012	34.9 ± 4.6	245–300	0.89	55	+0.50
NGC 4579	0.783 ± 0.008	94.8 ± 1.3	340–380	0.79	95	+0.54
NGC 4580[f]	0.712 ± 0.012	163.1 ± 1.5	115–140	0.78	165	−3.09
NGC 4593	0.742 ± 0.012	98.1 ± 4.6	260–330	0.74	55	+3.50
NGC 4618[f]	0.807 ± 0.008	36.6 ± 0.0	250–280	0.81	25	−1.68
NGC 4643	0.818 ± 0.012	56.0 ± 3.1	225–250	0.74	130	+2.40
NGC 4647[f]	0.663 ± 0.019	119.0 ± 1.2	220–240	0.79	125	−0.60
NGC 4651[f]	0.612 ± 0.127	73.1 ± 1.0	280–380	0.66	80	+0.53
NGC 4654	0.563 ± 0.017	123.1 ± 3.2	200–400	0.58	128	+0.65
NGC 4665	0.891 ± 0.013	102.6 ± 1.4	175–210	0.83	–	+2.65
NGC 4689	0.734 ± 0.027	167.4 ± 1.4	230–350	0.81	–	+0.66
NGC 4691[f]	0.842 ± 0.023	41.2 ± 3.8	210–290	0.81	15	+0.57
NGC 4698	0.566 ± 0.016	174.6 ± 1.6	280–420	0.62	170	+0.67
NGC 4699	0.720 ± 0.016	41.2 ± 3.4	190–300	0.69	45	+3.69
NGC 4772	0.503 ± 0.011	144.8 ± 1.5	120–200	0.50	147	+2.49
NGC 4775	0.912 ± 0.026	66.9 ± 7.9	130–190	0.93	–	+1.87
NGC 4781	0.452 ± 0.018	116.4 ± 2.3	150–280	0.45	120	+3.62
NGC 4900[f]	0.925 ± 0.015	96.1 ± 2.0	155–200	0.93	–	+0.55
NGC 4902	0.915 ± 0.033	81.4 ± 16.1	160–200	0.89	70	+3.54
NGC 4930	0.798 ± 0.005	55.0 ± 4.9	250–380	0.83	40	+3.51
NGC 4939	0.534 ± 0.007	4.5 ± 0.4	420–440	0.51	5	0.00
NGC 4941[f]	0.470 ± 0.007	15.9 ± 0.7	250–280	0.54	15	−1.09
NGC 4995[f]	0.616 ± 0.005	96.4 ± 1.0	140–160	0.66	92	−1.68
NGC 5005	0.444 ± 0.023	63.5 ± 0.6	180–300	0.48	65	+4.41

Table 1 – *continued*

Galaxy	$q \pm sd$ (B)	$\phi \pm sd$	Range (arcsec)	q (RC3)	ϕ (RC3)	dϕ
NGC 5054	0.612 ± 0.008	158.2 ± 0.5	320–380	0.58	155	−0.34
NGC 5085	0.909 ± 0.013	49.5 ± 5.7	300–320	0.87	38	−0.28
NGC 5101	0.934 ± 0.017	78.2 ± 4.1	310–330	0.85	–	−0.47
NGC 5121	0.819 ± 0.017	26.8 ± 1.7	93–112	0.78	36	+3.49
NGC 5247	0.831 ± 0.012	40.0 ± 3.1	420–470	0.87	20	+1.34
NGC 5248[d]	0.909 ± 0.036	104.0 ± 8.5	105–115	0.72	110	
NGC 5334	0.760 ± 0.012	10.7 ± 3.2	250–340	0.72	15	+1.86
NGC 5427	0.928 ± 0.013	154.0 ± 5.9	230–240	0.85	170	+0.15
NGC 5483[g]	0.886 ± 0.027	23.0 ± 7.7	210–250	0.91	25	+3.43
NGC 5643	0.898 ± 0.027	131.2 ± 13.5	240–380	0.87	–	0.00
NGC 5676	0.442 ± 0.005	45.6 ± 0.9	140–230	0.48	47	+2.57
NGC 5701	0.913 ± 0.018	52.0 ± 4.2	330–400	0.95	–	+3.65
NGC 5713	0.863 ± 0.029	3.9 ± 0.0	190–250	0.89	10	+1.67
NGC 5850	0.866 ± 0.024	181.6 ± 6.8	320–400	0.87	140	+2.99
NGC 5921	0.705 ± 0.013	130.9 ± 3.4	240–330	0.81	130	+4.36
NGC 5962[f]	0.660 ± 0.029	111.5 ± 3.5	160–250	0.71	110	+0.44
NGC 6215	0.954 ± 0.026	118.8 ± 10.8	130–170	0.83	78	+1.51
NGC 6221	0.654 ± 0.006	10.6 ± 0.2	285–320	0.69	5	−0.03
NGC 6300	0.693 ± 0.000	104.8 ± 0.6	370–480	0.66	118	−0.21
NGC 6384	0.646 ± 0.023	28.5 ± 1.9	300–500	0.66	30	+0.74
NGC 6753	0.852 ± 0.020	29.3 ± 2.0	160–210	0.87	30	+0.19
NGC 6782	0.898 ± 0.017	34.9 ± 4.4	160–210	0.66	45	+0.26
NGC 6902	0.836 ± 0.029	149.5 ± 16.0	250–280	0.69	153	−0.60
NGC 6907	0.876 ± 0.012	82.6 ± 4.0	175–200	0.81	46	−2.12
NGC 7083	0.553 ± 0.008	6.2 ± 1.9	240–300	0.60	5	−0.17
NGC 7205	0.515 ± 0.007	67.1 ± 1.4	210–350	0.50	73	−0.16
NGC 7213	0.944 ± 0.015	1.9 ± 6.5	280–370	0.89	–	−2.34
NGC 7217	0.861 ± 0.021	93.0 ± 2.8	190–250	0.83	95	0.00
NGC 7412	0.621 ± 0.023	52.4 ± 2.3	320–380	0.74	65	−0.07
NGC 7418	0.765 ± 0.008	132.5 ± 1.8	220–320	0.74	139	+0.23
NGC 7479	0.741 ± 0.018	35.7 ± 2.5	195–240	0.76	25	−0.04
NGC 7552	0.873 ± 0.027	169.9 ± 1.4	230–280	0.79	1	+0.21
NGC 7582	0.471 ± 0.007	152.9 ± 1.0	300–450	0.42	157	−2.31
NGC 7713	0.427 ± 0.007	171.7 ± 1.3	200–240	0.41	168	−0.06
NGC 7723	0.693 ± 0.010	38.5 ± 1.4	160–210	0.68	35	+1.65
NGC 7727	0.892 ± 0.014	158.1 ± 11.4	165–190	0.76	35	+1.65
NGC 7741	0.690 ± 0.020	161.9 ± 4.1	160–210	0.68	170	+1.47

[a]Manual determination. [b]From the outer ring. [c]The image field is too small for a good measurement. [d]The measurement was done using the H-band image. [e]The pixel size of the B image is 0.40 arcsec instead of 0.27 arcsec given in the image header. [f]The pixel size of the B image is 0.72 arcsec instead of 0.36 arcsec given in the image header. [g]The pixel size of the B image is 0.50 arcsec instead of 0.39 arcsec given in the image header.

of sources. The results show good agreement between our values and those of García-Gómez et al. (2004), with $|\Delta q|$ averaging less than 0.05 and with $|\Delta\phi|$ averaging less than 10° for $\langle q \rangle \leqslant 0.65$. The errors in position angle increase towards larger values of $\langle q \rangle$ in this comparison, as would be expected because the position angle is undefined for round galaxies. The comparisons with RC3 parameters show similar trends with some significant disagreements even at intermediate inclinations.

The position angles and inclinations in RC3 are given at distances corresponding to the surface brightness level of 25 mag arcsec^{-2}, whereas the B-band images by EFP typically reach the surface brightness of 26 mag arcsec^{-2}, which means that the images we use are deeper. This explains many of the disagreements between our measurements and those given in RC3. For some of the galaxies, the deviations from RC3 values are very large, of which examples are NGC 4593 and 4643. In these two cases ϕ in RC3 deviates even by 43° and 74° from our measurements, respectively. In the latter case, q also deviates quite significantly [q(RC3) = 0.74, q(meas) = 0.82]. Other examples are NGC 1300 and 1808, for which we use outer rings/pseudo-rings to estimate the orientation parameters. There is no doubt that when the galaxy inclinations are not insignificant, large errors in the position angles may have drastic consequences to the perturbation strengths. However, the uncertainties in the orientation parameters are not very important for galaxies seen in nearly face-on orientation.

4 TWO-DIMENSIONAL BULGE/DISC/BAR DECOMPOSITION

4.1 Decomposition method

The structural decomposition is needed for several purposes in this paper (see Section 5). For calculating non-axisymmetric forces, we use a method which requires information on the vertical scaleheight of the disc. However, as it cannot be measured directly for low-inclination galaxies, the radial scalelength of the disc is needed to

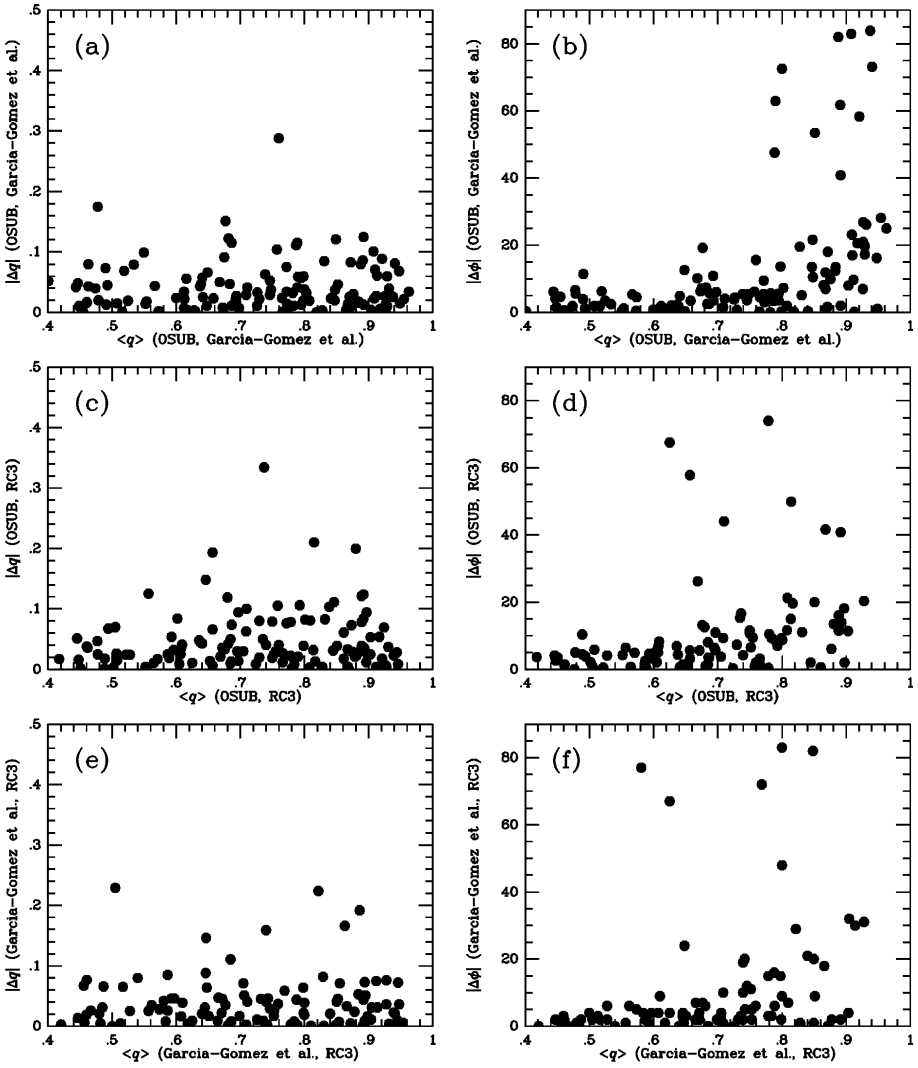

Figure 1. The orientation parameters measured in this study are compared with the RC3 values and with those obtained by García-Gómez et al. (2004). We plot the differences in the position angle $|\Delta\phi|$ and in the minor-to-major axial ratio $|\Delta q|$, versus the mean of q for each pair of sources. The two upper panels compare our values with those measured by García-Gómez et al., and the middle panels with the RC3 values. A comparison between RC3 values and those by García-Gómez et al. is shown in the lower panels.

estimate it indirectly. Also, while deprojecting the images, a bulge correction is applied, treating the bulges as separate structural components in galaxies.

In recent years, 2D decomposition methods have been widely used to separate structural components such as bulges and discs in galaxies. 2D methods are especially useful for separating non-axisymmetric structures, such as bars, ovals and rings, from the disc, but that advantage has only rarely been used (de Jong 1996; Peng 2002; Peng et al. 2002; de Souza, Gadotti & dos Anjos 2004). The first 2D methods used the $R^{1/4}$ law profile for the bulge (Shaw & Gilmore 1989; Byun & Freeman 1995; de Jong 1996; Wadadekar, Robbason & Kembavi 1999), whereas later studies have shown that the more general Sérsic $R^{1/n}$ function (Sérsic 1968) can better account for the bulge profiles in spiral galaxies. The Sérsic function has recently been used in conjunction with 2D decomposition methods by Möllenhoff & Heidt (2001, hereafter MH), Simard et al. (2002), Peng et al. (2002), MacArthur, Courteau & Holtzman (2003) and de Souza et al. (2004), all developed for different purposes. For example, the method of Simard et al. was developed for treating *Hubble Space Telescope* (*HST*) images with low signal-to-noise ratios, whereas the method of Peng et al. is suitable also for detailed structural analysis of nearby galaxies. In order to separate bars and discs from bulges, we use H-band images and 2D three-component decomposition. For our purposes, a reliable estimation of the bulge light distribution is important, because overestimating the bulge easily causes us to underestimate the bar strength, especially in early-type galaxies (see Section 5). Although bars can be easily identified in many galaxies, their fitting in the decompositions is sometimes complicated, because bars might have non-flattened central structures, and it is not always clear whether boxy/peanut-shaped structures in galaxies are bars or flattened bulges. We took the approach that both bars and ovals are fitted in the decomposition if they are visible in the original images, or if they can be detected by Fourier methods (see Section 5). For the inclination limit we use, possible boxy/peanut-shaped structures are mostly invisible. Some of the galaxies in our sample have bars made up of two components, a thin long bar and a thicker and shorter component, both of which were modelled as a single component. However, because the main

purpose for including a bar in the decomposition is to help to extract a more reliable bulge model, its exact treatment is not very crucial.

The bulge and the disc are described as in MH, using an exponential function for the disc and the $R^{1/n}$ Sérsic function for the bulge:

$$I_{\rm d}(r) = I_{0\rm d}\exp[-(r/h_r)],$$

$$I_{\rm b}(r) = I_{0\rm b}\exp[-(r/h_b)^{\beta}].$$

Here, h_r and h_b are the scale parameters of the disc and bulge, $I_{0\rm d}$ and $I_{0\rm b}$ are the central surface densities and $\beta = 1/n$ determines the slope of the projected surface brightness distribution of the bulge. For the disc, the radius r is calculated along the disc plane, whereas for the spherical bulge model, r is the projected distance from the centre. Special cases of the Sérsic function are the exponential function with $n = 1$ and the de Vaucouleurs function with $n = 4$. Additionally, a bar/oval component was added, described by a function

$$I_{\rm bar}(r) = I_{0\rm bar} * (1 - m^2)^{n_{\rm bar}+0.5},$$

where $m^2 = (x_{\rm b}/a)^2 + (y_{\rm b}/b)^2 < 1$, while a and b are the bar major and minor axes, $I_{0\rm bar}$ is the central surface brightness of the bar and $n_{\rm bar}$ is the exponent of the bar model. This corresponds to a projected surface density of a prolate Ferrers bar, with $a > b = c$, seen along the c-axis. Here $x_{\rm b}$ and $y_{\rm b}$ are coordinates in the disc plane in a system aligned with the bar major axis, making an angle $\phi_{\rm bar}$ with the nodal line of the disc. We generally used $n_{\rm bar} = 2$. Because bars sometimes have quite complicated structures, the Ferrers model is only an approximation of the true bar intensity distribution.

Iterative fits were performed on the images in magnitude units using a weighting function of $w_i = 1/r_i$, where r_i is the distance from the galaxy centre along the disc plane. This means that each radial zone has the same total weight. In Laurikainen & Salo (2000) we have shown that, in one dimension, unweighted magnitude fits (corresponding most closely to the adopted 2D weighting) are most stable, in a sense that the fit results were least affected by adding artificial noise to the profiles. In order to allow for seeing, the model bulge profile was convolved with a Gaussian (PSF) using the FWHM measured for each galaxy. The maximum radius used in the fit was taken to be the radius at which no negative pixels appeared in the image. This is important because the decompositions were performed with images converted to magnitude units. Generally, bars were fitted leaving the parameters describing the size, orientation ($a, b, \phi_{\rm bar}$) and the flux level of the bar ($I_{0\rm bar}$) free. However, when the surface brightness of the bar was close to that of the disc, the bar major axis had to be fixed, based on visual estimation in the original image. The total number of fitted parameters was nine, of which four describe the bar model. In galaxies with bright active galactic nuclei (AGN) the bulges were contaminated by the flux of the AGN in a region corresponding to the size of the seeing disc. In the H-band images, a typical PSF had a FWHM of 1.8 ± 0.3 arcsec, corresponding to the two innermost pixels in the galaxy centre. Spiral arms were not a major problem for the fits, because the arms are less prominent in the near-IR than in the optical.

The measured structural parameters are listed in Table 2, where the parameters $r_{\rm eff}$ and β describe the bulge and h_r is the exponential scalelength of the disc. The effective radius, $r_{\rm eff}$, is calculated from the scale parameter h_b of the bulge. The last column also denotes whether a bar/oval was fitted in the decomposition. If no bulge model is given in the table, the galaxy had no detectable bulge. A galaxy was considered to have no bulge if the azimuthally averaged surface density profile had no detectable bulge-like component outside the seeing disc and no Sérsic model could be fitted to the assumed

Table 2. Structural parameters from 2D decompositions. ':' after a value means that the measurement is uncertain.

Galaxy	$r_{\rm eff}$ (arcsec)	β	h_r (arcsec)	B/D	Bar/oval
OSUBGS					
ESO 138	8.822	0.495	43.8	0.098	
IC 4444	1.439	1.466	11.0	0.020	Bar/oval
IC 5325	1.887	1.223	21.4	0.017	Bar/oval
NGC 150	1.420	0.904	23.7	0.065	Bar/oval
NGC 157	1.847	1.418	25.0	0.022	
NGC 210[g]	3.928	0.770	132.1	0.309	Bar/oval
NGC 278	3.117	1.125	14.4	0.054	Bar/oval
NGC 289	2.346	1.062	19.1:	0.049	Bar/oval
NGC 428	0.982	0.483	26.7	0.002	Bar/oval
NGC 488	9.305	0.395	38.7	0.266	
NGC 578	1.860	1.559	39.5	0.011	Bar/oval
NGC 613	4.166	1.051	48.5	0.122	Bar/oval
NGC 685	2.104	1.408	40.4	0.007	Bar/oval
NGC 864	1.826	0.943	28.2	0.024	Bar/oval
NGC 908	3.021	0.583	40.9	0.052	
NGC 1042	2.184	0.775	42.8	0.019	Bar/oval
NGC 1058[e]	1.458:	1.857:	19.6:	0.017:	
NGC 1073	3.997	1.484	47.5	0.030	Bar/oval
NGC 1084	9.104	0.689	28.5	0.336	Bar/oval
NGC 1087	1.788	1.690	26.8	0.013	Bar/oval
NGC 1187	1.359	0.701	32.2	0.046	Bar/oval
NGC 1241	2.055	1.601	19.8	0.126	Bar/oval
NGC 1300[b]	3.407:	0.770:	74.3:	0.116:	Bar/oval
NGC 1302	10.664	0.275	45.8	0.580	Bar/oval
NGC 1309	2.279	0.970	10.9	0.065	
NGC 1317	4.346	0.670	26.0	0.420	Bar/oval
NGC 1350	4.899	0.732	79.3	0.215	Bar/oval
NGC 1371	3.319	0.834	27.2	0.111	Bar/oval
NGC 1385	16.195	0.904	37.0	0.563	Bar/oval
NGC 1493	1.249	0.513	29.9	0.006	Bar/oval
NGC 1559	–	–	22.4	–	Bar/oval
NGC 1617	4.075	0.697	33.9	0.169	Bar/oval
NGC 1637	2.119	0.723	29.9	0.058	Bar/oval
NGC 1703	1.927	1.165	19.7	0.033	Bar/oval
NGC 1792	2.106	1.100	33.7	0.024	
NGC 1808[a,g]	6.646:	0.385:	109.3:	0.595:	Bar/oval
NGC 1832	1.831	0.920	15.6	0.097	Bar/oval
NGC 2090[b]	2.053:	0.852:	18.9:	0.016(B)	
NGC 2139	20.225	0.448	18.5	0.546	Bar/oval
NGC 2196	6.291	0.508	20.7	0.415	
NGC 2207[e]	2.668:	1.153:	41.4:	0.171:	Bar/oval
NGC 2442[f]	5.281:	0.447:	153.5(B)	0.166:	Bar/oval
NGC 2559	2.589	1.275	26.2	0.056	Bar/oval
NGC 2566	2.470	0.434	90.2	0.141:	Bar/oval
NGC 2775	20.274	0.358	43.1	0.931	
NGC 2964	1.405	1.043	19.9	0.064	Bar/oval
NGC 3059	1.891	1.903	28.8	0.015	Bar/oval
NGC 3166	4.547	0.594	39.6	0.554	Bar/oval
NGC 3169	6.863	0.569	32.5	0.779	
NGC 3223	5.528	0.473	30.8	0.147	
NGC 3227[b]	1.811	0.450	26.1:	0.177	Bar/oval
NGC 3261	2.743	0.881	22.0	0.243	Bar/oval
NGC 3275	2.893	0.750	23.2	0.211	Bar/oval
NGC 3319	2.036	1.427	60.8	0.006	Bar/oval
NGC 3338	20.647	0.222	33.4	0.290	Bar/oval
NGC 3423	4.555	0.873	33.0	0.033	Bar/oval
NGC 3504	2.651	0.997	27.8	0.356	Bar/oval
NGC 3507	2.363	0.633	26.3	0.072	Bar/oval
NGC 3513	1.678	2.077	27.2	0.007	Bar/oval
NGC 3583	2.078	0.853	17.8	0.122	Bar/oval
NGC 3593	4.097	0.712	30.1	0.161	Bar/oval
NGC 3596	1.777	0.740	20.3	0.047	Bar/oval

Table 2 – *continued*

Galaxy	$r_{\rm eff}$ (arcsec)	β	h_r (arcsec)	B/D	Bar/oval
NGC 3646	2.849	0.525	24.5	0.168	
NGC 3675	13.362	0.231	41.0	0.230	Bar/oval
NGC 3681	1.457	1.250	12.2	0.066	Bar/oval
NGC 3684	1.405	0.591	13.3	0.022	Bar/oval
NGC 3686	1.673	1.126	25.4	0.020	Bar/oval
NGC 3726	1.205	0.747	46.4	0.009	Bar/oval
NGC 3810	10.697	0.761	29.6	0.453	
NGC 3887	2.375	1.111	34.7	0.019	Bar/oval
NGC 3893	19.939	0.463	34.2	–	
NGC 3938	5.636	0.610	32.3:	0.053	Bar/oval
NGC 3949[b]	4.942:	0.737:	14.1(B)	0.133	
NGC 4027	1.412	3.626	26.0	–	Bar/oval
NGC 4030	9.761	0.497	22.7	0.300	Bar/oval
NGC 4051[b]	3.220:	0.314:	70.0:	0.141:	Bar/oval
NGC 4123	2.308	0.760	31.4	0.090	Bar/oval
NGC 4136	2.122	0.642	25.7	0.019	Bar/oval
NGC 4138	4.013	0.371	17.4	0.298	
NGC 4145	–	–	57.9	–	Bar/oval
NGC 4151[b]	4.293:	0.516:	27.1(B)	0.758:	Bar/oval
NGC 4212	2.358	1.175	21.9	0.044	Bar/oval
NGC 4242	3.535	0.569	53.4	0.003	
NGC 4254	9.814	0.700	33.5	0.151	
NGC 4293	4.646	0.698	52.3	0.077	Bar/oval
NGC 4303	2.956	1.093	42.4	0.085	Bar/oval
NGC 4314	5.461	0.791	51.1	0.190	Bar/oval
NGC 4394	3.821	0.740	33.4	0.215	Bar/oval
NGC 4414	10.872	0.290	24.1	0.524	
NGC 4450	4.836	0.563	43.6	0.145	Bar/oval
NGC 4457	4.283	0.556	28.5	0.733	Bar/oval
NGC 4487	29.140:	0.206:	31.6:	0.099:	Bar/oval
NGC 4490	–	–	37.6	–	Bar/oval
NGC 4496A	–	–	30.8	–	Bar/oval
NGC 4504[b]	4.155:	0.441:	22.9(B)	0.011:	Bar/oval
NGC 4527	3.776	0.788	38.9	0.243	Bar/oval
NGC 4548	6.118	0.589	59.5	0.176	Bar/oval
NGC 4571	2.947	1.253	35.4	0.011	Bar/oval
NGC 4579	4.538	0.691	41.8	0.155	Bar/oval
NGC 4580	1.602	2.928	16.9	0.010	
NGC 4593	4.317	0.673	56.6	0.271	Bar/oval
NGC 4618	26.681:	0.455:	32.2:	0.109:	Bar/oval
NGC 4643	6.412	0.727	46.1	0.431	Bar/oval
NGC 4647	20.695	0.477	27.7	0.395	
NGC 4651	17.215	0.377	26.4	0.553	Bar/oval
NGC 4654	2.102	0.757	30.9	0.012	Bar/oval
NGC 4665	5.578	0.932	39.4	0.198	Bar/oval
NGC 4689	4.770	1.032	36.4	0.042	
NGC 4691	3.455	1.365	30.9	0.065	Bar/oval
NGC 4698[b]	12.918:	0.345:	43.5(B)	0.691:	Bar/oval
NGC 4699	6.122	0.458	21.1	0.509	Bar/oval
NGC 4772	7.196	0.581	42.7	0.513	
NGC 4775	4.090	1.461	16.0	0.038	
NGC 4781	12.379	0.486	29.4	0.069	Bar/oval
NGC 4900[c]	2.702:	1.227:	14.5:	0.019:	Bar/oval
NGC 4902	2.862	1.010	22.1	0.086	Bar/oval
NGC 4930[b]	3.641:	0.788:	36.8(B)	0.237:	Bar/oval
NGC 4939	14.099	0.403	40.6	0.379	Bar/oval
NGC 4941	2.474	0.705	30.3	0.142	
NGC 4995	1.415	0.997	18.3	0.051	Bar/oval
NGC 5005	3.029	0.686	34.1	0.144	Bar/oval
NGC 5054	4.839	0.404	42.5	0.173	
NGC 5085	3.867	1.095	26.9	0.050	
NGC 5101	11.469	0.350	100.0	0.495	Bar/oval
NGC 5121	2.568	0.622	13.4	0.372	

Table 2 – *continued*

Galaxy	$r_{\rm eff}$ (arcsec)	β	h_r (arcsec)	B/D	Bar/oval
NGC 5247	8.313	0.804	62.7	0.096	
NGC 5248	7.010	0.696	71.3	0.287	Bar/oval
NGC 5334	0.602	0.785	32.5	0.001	Bar/oval
NGC 5427	3.418	1.080	19.1	0.081	
NGC 5483	6.438	1.434	24.0	0.082	Bar/oval
NGC 5643	2.588	0.552	39.7	0.069	Bar/oval
NGC 5676	1.973	1.078	21.1	0.045	
NGC 5701[2,7]	7.078:	0.439:	32.6(B)	0.352:	Bar/oval
NGC 5713	2.112	1.504	18.5	0.051	Bar/oval
NGC 5850	4.912	0.769	58.4	0.208	Bar/oval
NGC 5921	2.331	0.863	35.7	0.108	Bar/oval
NGC 5962	4.549	0.383	17.6:	0.213	Bar/oval
NGC 6215	2.651	0.828	15.5	0.083	
NGC 6221	2.715	0.702	32.6	0.086	Bar/oval
NGC 6300	3.467	0.656	39.6	0.050	Bar/oval
NGC 6384	7.149	0.385	40.3	0.148	Bar/oval
NGC 6753	6.171	0.593	22.7	0.397	Bar/oval
NGC 6782	3.193	1.019	26.5	0.319	Bar/oval
NGC 6902	3.066	0.794	33.1	0.131	Bar/oval
NGC 6907	5.230	0.694	23.9	0.184	Bar/oval
NGC 7083	4.989	0.516	20.0	0.150	
NGC 7205	1.262	0.889	27.0	0.021	Bar/oval
NGC 7213	15.330	0.363	54.3	1.472	
NGC 7217	18.423	0.401	32.7	0.852	
NGC 7412[d]	4.272	0.691	32.2	0.051	
NGC 7418	1.279	0.576	43.5	0.017	Bar/oval
NGC 7479	3.397	0.967	39.6	0.069	Bar/oval
NGC 7552	3.971	0.685	59.1	0.435	Bar/oval
NGC 7582	1.760	0.454	45.1	0.178	Bar/oval
NGC 7713	34.353	0.355	37.8	0.056	Bar/oval
NGC 7723	1.770	1.220	20.9	0.046	Bar/oval
NGC 7727	8.059	0.330	22.5	0.669	Bar/oval
NGC 7741[a] 2MASS	–	–	37.5	–	Bar/oval
NGC 772	24.311	0.320	49.6	0.713	
NGC 1068	1.923	0.817	20.7	0.128	Bar/oval
NGC 1097	7.297	0.740	25.0	0.241	Bar/oval
NGC 1232	5.034	0.484	35.8	0.029	Bar/oval
NGC 1398	8.071	0.524	38.0	0.371	Bar/oval
NGC 2655	8.947	0.519	28.0	0.811	
NGC 2841	6.323	0.566	50.8	0.195	
NGC 2985	10.596:	0.413:	26.1(MH)	0.685:	Bar/oval
NGC 3031	10.915	0.498	57.1	0.337	
NGC 3077	8.898	0.681	33.1	0.110	
NGC 3486	2.771	0.977	18.0	0.120	
NGC 3521	2.462	0.506	37.2	0.087	Bar/oval
NGC 3718	7.219	0.376	27.7	0.487	
NGC 3898	3.420	0.524	26.0	0.326	Bar/oval
NGC 4321	8.623:	0.560:	49.5(MH)	0.096:	Bar/oval
NGC 4501	3.388:	0.512:	42.3(MH)	0.049:	Bar/oval
NGC 4569	3.933	0.445	61.5	0.143	Bar/oval
NGC 4736	14.586	0.573	58.3	1.007	Bar/oval
NGC 4753	14.914	0.330	38.4	0.934	
NGC 5457	29.366	0.385	112.8	0.081	
NGC 6643	1.910	2.243	23.9	0.019	
NGC 7513	3.776	1.289	58.0	0.032	Bar/oval

[a]Manual decomposition fit. [b]H-band image not deep enough to determine h_r well, but the bulge model is reasonable. [c]Bulge model is taken from the fit to the inner regions, and the disc parameters from the fit to the outer regions of the galaxy. [d]No bar is fitted, although the galaxy is barred in RC3. [e]The number of iterations is limited in the decomposition. [f]The H-band image field is too small. [g]Prominent outer ring dominates the disc.

bulge region (unclear cases are discussed in Section 4.2). In order to estimate the relative mass of the bulge properly, the bulge model was always taken from the decompositions made for the H-band images. However, when the H-band images were not deep enough for reliable estimation of the scalelength of the disc, h_r was estimated from the decompositions applied to the deeper B-band images. Also, for three of the galaxies in the 2MASS sample, h_r given by MH was used. Some examples of the decompositions are shown in Fig. 2 (Fig. 2b is available in the online version of this paper).

4.2 Discussion of the sample galaxies

The main limitation of our decompositions is that not all H-band images were deep enough for detecting the outermost parts of the discs, which is the case for the galaxies NGC 1300, 1808, 2090, 3227, 3949, 4051, 4151, 4504, 4698, 4930 and 5701. However, even for these galaxies a large fraction of the exponential disc was still visible, so that the bulge could be separated from the disc quite well. The image field was slightly smaller than the size of the galaxy for NGC 2442, which made it difficult to derive a reliable radial scalelength for this galaxy. Fitting was generally made using an automatic procedure, but for some of the galaxies it led to unphysical results. For example, for NGC 1058 it was possible to obtain a reasonable fit with either a small or a large bulge, both having similar global χ^2, describing the difference between the model image and the observed image. A similar case is shown also by Mac Arthur et al. (2003) (see their fig. 9). While MacArthur et al. solved the problem by computing separate inner and outer χ^2 residuals, we limited the number of iterations so that the physically unreasonably large bulge would be avoided. Also, for galaxies such as NGC 210, 1808 and 5701, having prominent outer rings complicates the interpretation of the structural decomposition. We have found that including a bar in the decomposition can significantly modify the scale parameters of the bulge and the disc, so that ignoring a bar model in the decomposition would overestimate the B/D ratio and the shape parameter n of the bulge. Also, if the bar is very prominent, ignoring a bar model would overestimate the scalelength of the disc.

In the following we discuss some individual cases.

NGC 1187 and 1302 (see Fig. 2a). In the case of NGC 1187, in which the bar is small, including a bar component to the decomposition decreases the shape parameter of the bulge from $n = 2.0$ to 1.4, thus making the bulge profile appear more exponential. Consequently, the total flux of the bulge is decreased by 30 per cent. However, the disc model is not affected. An example of a galaxy with a larger bar is NGC 1302, for which inclusion of the bar affects not only the fitted bulge, but also the radial scalelength of the disc, which is reduced by 12 per cent. The bar resides inside a roundish inner ring and is prominent in the bulge-dominated region of the galaxy. For this galaxy, the bulge/disc decomposition without any bar model would overestimate the mass of the bulge by as much as 36 per cent. The effect of the bar model in the decomposition for NGC 1302 is demonstrated in a different manner in Fig. 3. Two residual images are shown for two different decompositions: in one image the bulge model is subtracted from the original image, whereas in the other image the whole galaxy model is subtracted. It is clear that if no bar model is included in the decomposition the bulge model becomes too large, mainly because a considerable amount of bar flux is assigned to the bulge.

NGC 210. This galaxy has a bar whose surface brightness is high in comparison with that of the underlying disc, which is dominated by an outer pseudo-ring. Because of the prominent bar, it is not possible to perform any reliable decomposition for this galaxy without also modelling the bar (which in blue light is a well-known SAB-type oval). However, the prominence of the outer ring made decompositions problematic. In fact, this is true for outer-ringed galaxies in general.

NGC 3166, 4699, 4939, 5701 and 6394. For these galaxies the bar resides mostly inside the large bulge, of which NGC 3166 and 4699 are shown as examples in Fig. 2. The bars are so strong that, for example, for NGC 4699, according to our decomposition model, the surface brightnesses of the bar and the bulge are nearly the same at the edge of the bar. It is clear that in these galaxies ignoring the bar would overestimate the B/D ratio.

NGC 6902. In most cases, a bar can be detected in the surface brightness profile of the galaxy, but for NGC 6902 the bar is too weak to appear as a bump in the profile. However, the bar is visible by eye in the original image (inside a prominent inner ring at $r <$ 10 arcsec; see also Crocker, Baugus & Buta 1996) and is detectable also by Fourier methods. In this galaxy, the prominent bump visible in the surface brightness profile at $r = 10$–40 arcsec is due to an oval, which was modelled by a Ferrer function.

NGC 1084, 4698, 4962, 5962 and 6753. There are some non-barred galaxies in the sample whose decompositions were improved by modelling ovals by a Ferrers function. As an example the decomposition for NGC 6753 is shown in Fig. 2(b) (see the online version). In this case, the oval has a relatively low surface brightness and cannot be directly distinguished in the profile. However, it is prominent in direct images and divides the zone between bright nuclear and outer rings (see Crocker et al. 1996).

The decomposition remained unsatisfactory for the galaxies NGC 4487, 4900, 2139 and 4618. Characteristic for all these galaxies is that they have little or no bulge, or that the bulge has very low surface brightness in comparison with that of the disc. As an example, the decomposition of NGC 4487 is shown in Fig. 2(b) (the online version). For this galaxy, the bulge model has a very large shape parameter ($n = 5$), which appears immediately after giving the initial parameters of the fit. Such a centrally peaked extended bulge is the only solution for this galaxy, but it is not clear whether the solution is physically reasonable. At least it is not intuitively expected in the profile, where the bulge does not look very prominent. Among the sample galaxies there is also one galaxy, NGC 4900, having a strong Freeman type II profile, which makes it impossible to fit any usual global disc model, unless a truncated disc is assumed. In this study, the radial scalelength of the disc for this galaxy was estimated from the outer regions of the disc, whereas the bulge model was extracted using the inner portions of the image. The decomposition was uncertain also for the two late-type spirals, NGC 2139 and 4618, both having an asymmetric disc. NGC 4618 is a prototypical one-armed SBm spiral (de Vaucouleurs & Freeman 1972) and most probably has no bulge at all.

4.3 Comparison with previous studies

In spite of the widespread use of the decomposition technique for the derivation of the structural parameters of spiral galaxies, it is difficult to find sufficient published data to make a comparison with our results. One reason is that it has only recently been shown that no single shape parameter can describe the bulges of all spiral galaxies. Also, although 2D methods are widely used, there has been no previous study like ours, where bulge/disc/bar decomposition, using both the generalized Sérsic model for the bulge and a separate model for the bar, has been applied to a large sample of galaxies.

In the following, we compare our results with those obtained by MH, who use a two-component 2D method, and with Knapen

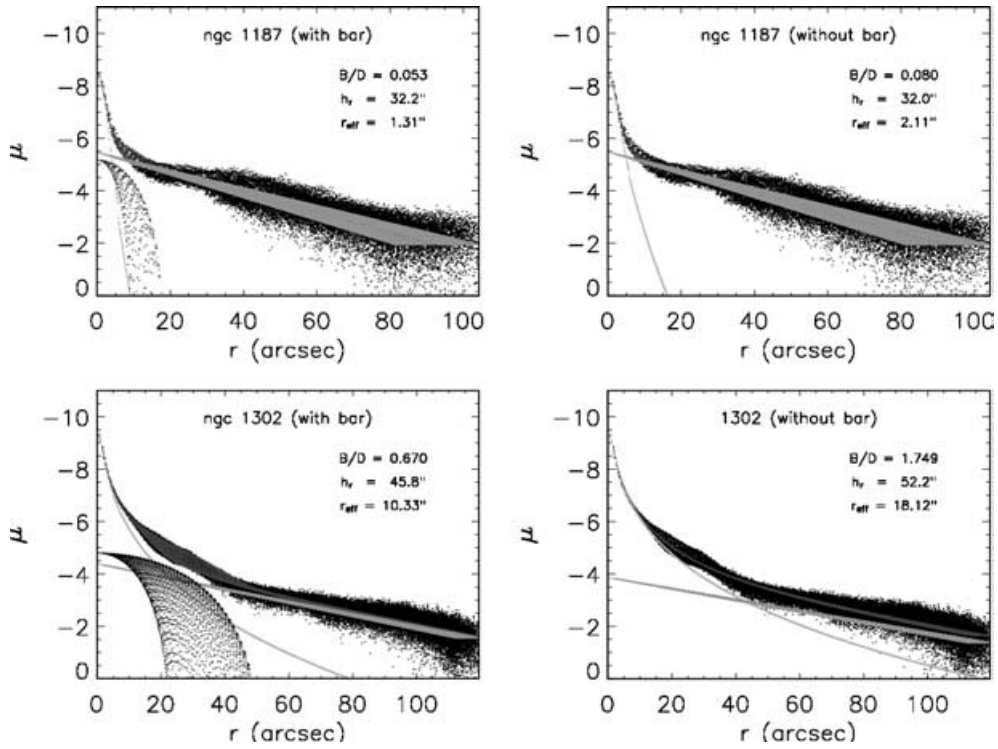

Figure 2. (Fig. 2b can be found in the online version of this paper at http://www.blackwellpublishing.com/products/journals/suppmat/MNR/MNR8410/MNR8410sm.htm.) Decomposition results using a 2D method, where the discs are modelled by an exponential function, the bulges using the generalized Sérsic model, and bars by a Ferrer function. The observed brightness of each pixel is shown versus its distance from the centre, measured in the sky plane (black points), and the corresponding model components: bulge (grey points falling on a curve), disc (grey points in a wedge-shaped region) and bar (points in a region limited by two curves). The total model is shown by dark grey points on top of observations. As no flux calibration was performed, the magnitude scale in the *y*-axis has an arbitrary zero-point. In (a) the effect of including/excluding the bar model in the decomposition is shown for NGC 1187 and 1302, while (b) shows other selected cases discussed in the text.

et al. (2003) using a two-component one-dimensional (1D) method. In both studies, the observations are made in the near-IR with subarcsec image resolution, and also the surface brightness profiles were modelled using an exponential function for the disc and Sérsic function for the bulge. A typical limiting surface brightness in the study by Knapen et al. was 20.5 mag arcsec^{-2} in the K band, which is similar to that in our sample in the H band (20 mag arcsec^{-2}), whereas the limiting magnitude by MH was not given.

We have 13 galaxies in common with the sample by MH. For eight of the galaxies, the bulge/disc parameters were very similar in both studies. Dividing the parameter value measured by us by the value given in MH, and taking a mean of the measurements for different galaxies, we found $\langle r_e/r_e(\mathrm{MH})\rangle = 0.81 \pm 0.27$, $\langle n\ /n(\mathrm{MH})\rangle = 1.04 \pm 0.50$, and $\langle h_r/h_r(\mathrm{MH})\rangle = 1.02 \pm 0.19$, where the uncertainties are standard deviations of the mean of the measured ratios. However, for the remaining five galaxies the bulge and/or disc parameters obtained by MH deviated significantly from our values. For two of these, NGC 4450 (see Fig. 2 in the online version) and 4051, the inclusion of a bar is the likely explanation for the different results. The bar is very large in NGC 4051 and including it in the decomposition makes the underlying exponential disc also large ($h_r = 70.0$ arcsec versus 49.6 arcsec). In NGC 4450, the bar is smaller and therefore does not affect h_r, which is also found to be similar in the two studies. However, fitting a bar for this galaxy affects the bulge model, thus making it more exponential ($n = 3.6$–1.8). The decomposition parameters are also different in the two studies for NGC 5248, for which we measure a much smaller h_r than MH ($h_r = 71.3$ arcsec versus 194.1 arcsec), and for the two non-barred galaxies, NGC 4254 and 2196.

With the sample by Knapen et al. we have 14 galaxies in common. In spite of the 1D nature of their decomposition, even in this case for half of the galaxies they measure similar structural parameters as obtained by us. For these galaxies $\langle r_e/r_e\ (\mathrm{Knapen})\rangle = 0.80 \pm 0.30$, $\langle n/n(\mathrm{Knapen})\rangle = 1.03 \pm 0.28$ and $\langle h_r/h_r(\mathrm{Knapen})\rangle = 1.02 \pm 0.20$. However, again, for half of the galaxies the structural parameters are quite different. This is the case for NGC 864, 4051, 5850 and 5921, for which the differences can be explained by the bar. For example, NGC 864 (shown in Fig. 2, online version) and 5921 have small bars that affect the bulges, whereas large bars in NGC 4051 and 5850 modify also the exponential discs. The parameters are somewhat different also for the non-barred galaxies NGC 4689, 5247 and 2775. For example, for NGC 2775 we measure a significantly larger h_r than Knapen et al. ($h_r = 43.1$ arcsec versus 26.2 arcsec), but the value we obtain is similar to that obtained by MH ($h_r =$ 44.3 arcsec).

As expected, the structural parameters derived from two-component models quite often disagree with the parameters derived using three-component models: fitting a large bar in the decomposition increases h_r and modifies the bulge model, while fitting a small bar only makes the shape of the bulge appear more exponential. However, bars do not explain all the differences found between the various studies; also, the image quality may easily affect the decomposition results.

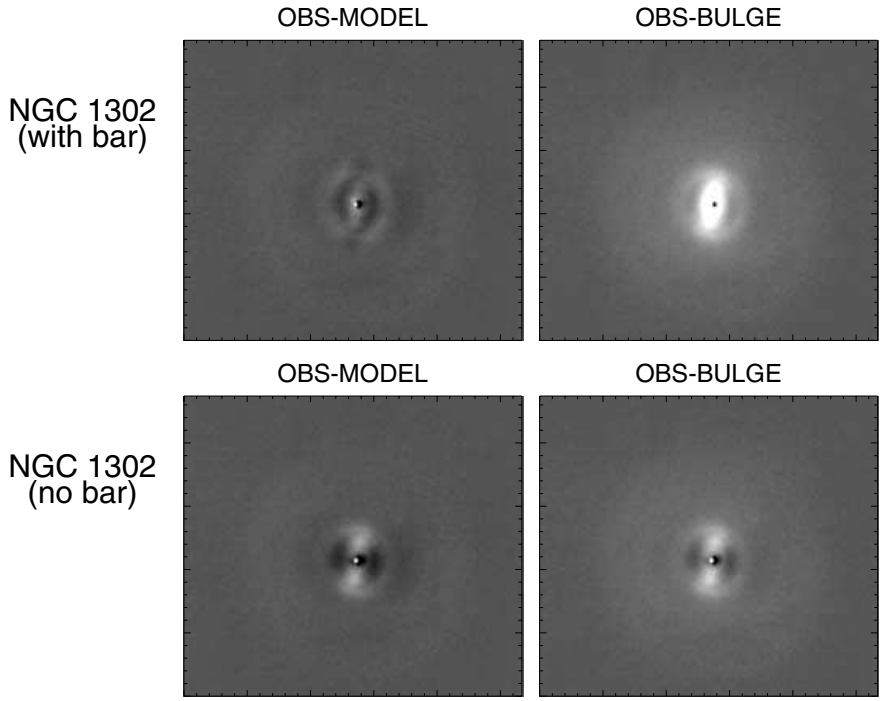

Figure 3. Images related to decomposition of NGC 1302; in the upper row, a bar component is included to the decomposition whereas in the lower row it is ignored. The frames show the residual images where the bulge model is subtracted from the original image (right), and when the complete galaxy model is subtracted (left).

5 METHOD FOR CALCULATING THE PERTURBATION STRENGTHS

Perturbation strengths induced by non-axisymmetric structures in galactic discs are calculated using the gravitational torque method (GTM), which quantifies bar and spiral strengths using a simple force ratio (Sanders & Tubbs 1980; Combes & Sanders 1981) based on gravitational potentials inferred from near-IR light distributions. BB first applied the GTM to a large sample of galaxies using a Cartesian potential evaluation (Quillen, Frogel & Gonzalez 1994). Here, we instead use a polar grid approach to infer the potentials, mainly because it reduces the noise, thus better taking into account the faint outer parts of the images. The method is explained and applied to a large sample of 2MASS images by LS. The polar approach was initially applied by Salo et al. (1999) to an early-type ringed barred spiral IC 4214. The refined method used in this study is explained in detail by Salo, Buta & Laurikainen (in preparation). The analysis provides 2D maps of radial ($F_{\rm R}$) and tangential ($F_{\rm T}$) forces in the galaxy plane. A radial profile of the maximum relative tangential force at each distance is calculated as

$$Q_{\rm T}(r) = \frac{|F_{\rm T}(r,\phi)|_{\rm max}}{\langle |F_{\rm R}(r,\phi)| \rangle},$$

where $\langle |F_{\rm R}(r,\phi)| \rangle$ denotes the azimuthally averaged axisymmetric force at each radius. While constructing $|F_{\rm T}|_{\rm max}$ at each radius, we use the mean of the maximum $|F_{\rm T}|$ over azimuth found separately in four different image quadrants. The maximum in the radial $Q_{\rm T}$ profile then gives a single measure of bar strength, $Q_{\rm g}$, which is equivalent to the maximum gravitational bar torque per unit mass per unit square of the circular speed. Another useful parameter is $r_{Q_{\rm g}}$, which gives the radial distance of the maximum perturbation strength. $Q_{\rm g}$ is generally associated with a bar, but in some cases it can also be related to spiral arms. It is also possible that the bar and the spiral are partially overlapping in some galaxies, and a method to separate the two components, based on Fourier techniques, has been developed by Buta, Block & Knapen (2003).

The bar-induced gravitational potential is calculated from a deprojected H-band image using generally 10 even Fourier components, but the effect of the higher-order modes on $Q_{\rm g}$ was also tested. Because we were able to decompose the bulges from the discs and bars, the deprojected images are not affected by the bulge 'deprojection stretch' that would affect the inner regions if one were to assume that the bulge and disc have the same flattening. The bulge model is subtracted from the sky-plane image, the disc is deprojected to face-on orientation, and the radial contribution of the force is added back by assuming that the bulge is spherically symmetric. Also, this contribution is calculated from the analytical bulge model, corresponding to the seeing-deconvolved bulge image. The deprojections were made using the orientation parameters derived from the B-band images (see Section 3). The deprojected images for all the sample galaxies are shown in Fig. 4 (Figs 4b–e are available in the online version of the paper). These images are logarithmic, sky-subtracted, and in units of mag arcsec^{-2} with an arbitrary zero-point. The scales are all different and the displays are designed to show as much information as possible over a full range of surface brightness.

The main assumptions of the GTM are that the near-IR light distribution traces the mass of the galaxy, that the mass-to-luminosity ratio is constant in all parts of the discs in the H band, and that the vertical density distribution of the disc can be represented by some simple function such as an exponential. The scaleheight h_z was estimated from the empirical correlation between h_r/h_z and the de Vaucouleurs type index T given in RC3 (de Grijs 1998). The measurements for the barred galaxies are shown in Table 3 and those for the non-barred galaxies are shown in Table 4, where the errors are

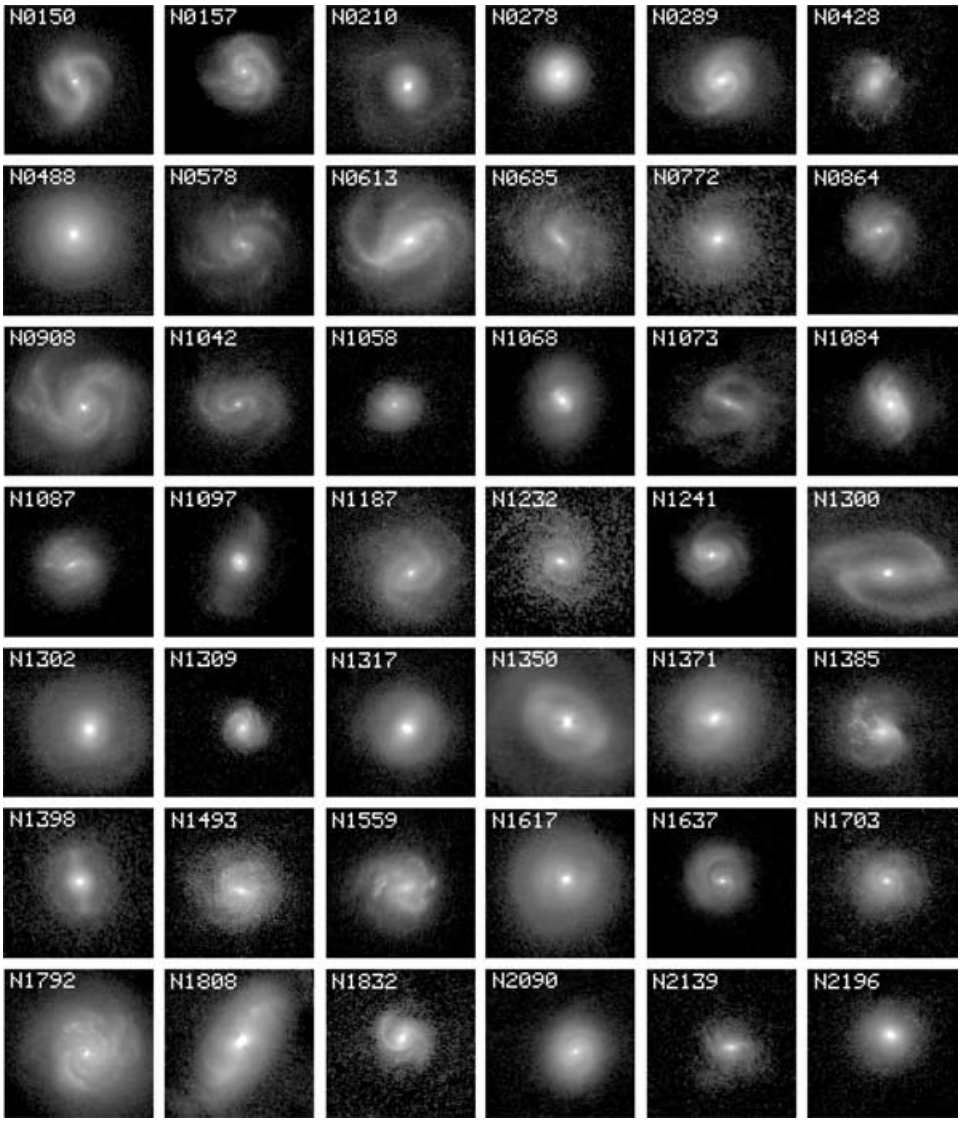

Figure 4. (Figs 4b and c can be found in the online version of this paper at http://www.blackwellpublishing.com/products/journals/suppmat/MNR/MNR8410/MNR8410sm.htm.) The deprojected images for the whole sample. The images are logarithmic, sky-subtracted, and in units of mag arcsec^{-2} with an arbitrary zero-point.

standard deviations of the measurements calculated in the four image quadrants. In Table 3 we also give the distance of the maximum $Q_{\rm T}$ ($r_{Q_{\rm g}}$), and the maximum $m = 2$ (A_2) and $m = 4$ (A_4) density amplitudes in the bar region. If the galaxy has a bar and some other $Q_{\rm T}$ maximum due to the spiral arms well outside the bar, the value corresponding to the bar is given in the table. The Fourier method enables us also to estimate the length of the bar, $r_{\rm bar}$, based on the phases of the $m = 2$ and $m = 4$ density amplitudes; the length of the bar was taken to be the radius at which the $m = 2$ and $m = 4$ phases were maintained nearly constant in the bar region. The length of the bar is given for the galaxies for which a bar was identified by Fourier methods, as explained in Section 6.

The last column in the table lists the visual bar classifications in the H band (EFP) and the bar classifications given in RC3. The radial $Q_{\rm T}$ profiles for all galaxies in the sample are shown in Fig. 5 (Figs 5b–h are available in the online version of this paper).

The uncertainties related to the bar torque method have been discussed in several previous papers. The method was found to be rather insensitive to the functional form of the vertical density distribution (LS), to the contribution of the dark matter halo (BLS), and to the radial variations in the vertical scaleheight (LS). At most, each of these factors can affect $Q_{\rm g}$ only by $\approx$5 per cent. BLS also studied how the position angle of the bar, relative to the line of nodes, could modify $Q_{\rm g}$; they found that $Q_{\rm g}$ is slightly weaker for the galaxies where the bar becomes 'thicker' in deprojection. Also, bars can be partly superimposed with the spiral arms, which can lead to an uncertainty of about 4 per cent on $Q_{\rm g}$ (Buta et al. 2003). However, more important sources of error are the vertical scaleheight of the disc, which can be estimated only indirectly from observations, and the uncertainties in the orientation parameters, which both can account for uncertainties in $Q_{\rm g}$ as much as 10–15 per cent (BLS; LS).

In the following we take a statistical approach and evaluate how much $Q_{\rm g}$ is affected on average, if the uncertainties in the orientation parameters, in the vertical scaleheights and in the number of Fourier modes included in the calculation are taken into account.

Table 3. Galaxies with Fourier bars.

Galaxy	Q_g	r_{Q_g} (arcsec)	Bar length (arcsec)	A_2	A_4	EFP/RC3	
OSUBGS							
IC 4444	0.254 ± 0.033	5.5	22.2	0.300	0.180	(B) (X)	
IC 5325	0.219 ± 0.020	12.7	23.2	0.280	0.140	(X) (X)	
NGC 150	0.459 ± 0.085	26.7	29.0	0.616	0.249	(B) (B)	
NGC 210	0.061 ± 0.001	36.0	46.0	0.413	0.106	(B) (X)	
NGC 289	0.212 ± 0.003	12.8	19.7	0.388	0.106	(B) (B)	
NGC 428	0.251 ± 0.020	28.5	45.0	0.437	0.076	(B) (X)	
NGC 578	0.182 ± 0.014	10.4	19.7	0.277	0.053	(B) (X)	
NGC 613	0.401 ± 0.045	68.4	104.4	0.754	0.479	(B) (B)	
NGC 685	0.424 ± 0.012	10.4	20.9	0.400	0.153	(B) (X)	
NGC 864	0.360 ± 0.037	19.5	25.5	0.438	0.155	(B) (X)	
NGC 1073	0.607 ± 0.013	25.5	37.5	0.703	0.313	(B) (B)	
NGC 1087	0.442 ± 0.020	7.5	18.0	0.440	0.172	(B) (X)	
NGC 1187	0.207 ± 0.043	36.0	29.0	0.345	0.123	(B) (B)	
NGC 1241	0.251 ± 0.028	22.5	30.0	0.410	0.136	(B) (B)	
NGC 1300	0.537 ± 0.011	68.4	87.0	0.743	0.348	(B) (B)	
NGC 1302	0.075 ± 0.006	24.4	25.5	0.303	0.066	(B) (B)	
NGC 1317	0.085 ± 0.007	40.6	58.0	0.334	0.102	(B) (X)	+ minibar
NGC 1350	0.243 ± 0.039	68.4	81.2	0.713	0.207	(B) (B)	+ minibar
NGC 1385	0.319 ± 0.030	3.5	9.3	0.266	0.196	(B) (B)	
NGC 1493	0.363 ± 0.010	10.4	23.2	0.304	0.137	(B) (B)	
NGC 1559	0.334 ± 0.001	5.8	17.4	0.246	0.102	(B) (B)	
NGC 1617	0.079 ± 0.027	7.8	22.2	0.600	0.200	(X) (B)	
NGC 1637	0.202 ± 0.014	16.5	22.5	0.350	0.137	(B) (X)	
NGC 1703	0.100 ± 0.005	8.9	11.1	0.184	0.070	(X) (B)	
NGC 1808	0.274 ± 0.001	77.7	87.0	1.102	0.586	(B) (X)	+ minibar
NGC 1832	0.195 ± 0.024	12.2	16.6	0.405	0.166	(B) (B)	
NGC 2139	0.398 ± 0.032	3.3	16.6	0.380	0.139	(B) (X)	
NGC 2207	0.317 ± 0.032	29.0	46.4	0.700	0.350	(B) (X)	
NGC 2442	0.669 ± 0.428	77.7	92.8	0.979	0.421	(B) (X)	
NGC 2559	0.316 ± 0.039	27.8	33.3	0.512	0.151	(B) (B)	
NGC 2566	0.316 ± 0.069	54.4	72.1	0.865	0.391	(B) (B)	
NGC 2964	0.310 ± 0.003	22.5	30.0	0.419	0.223	(X) (X)	
NGC 3059	0.544 ± 0.048	7.8	20.0	0.727	0.359	(B) (B)	
NGC 3166	0.107 ± 0.019	31.5	45.0	0.524	0.221	(B) (X)	+ oval/minibar
NGC 3227	0.158 ± 0.021	55.5	75.0	0.444	0.272	(B) (X)	
NGC 3261	0.196 ± 0.009	18.9	27.7	0.538	0.233	(B) (B)	
NGC 3275	0.187 ± 0.013	23.3	41.1	0.533	0.214	(B) (B)	
NGC 3319	0.542 ± 0.019	13.5	37.5	0.630	0.250	(B) (B)	
NGC 3338	0.083 ± 0.005	13.5	22.5	0.118	0.054	(X) (A)	
NGC 3504	0.288 ± 0.030	28.5	60.0	0.991	0.476	(B) (X)	
NGC 3507	0.176 ± 0.005	19.5	22.5	0.379	0.107	(B) (B)	
NGC 3513	0.541 ± 0.069	14.4	27.7	0.429	0.226	(B) (B)	
NGC 3583	0.246 ± 0.006	16.5	22.5	0.649	0.203	(B) (B)	
NGC 3593	0.152 ± 0.002	10.5	15.0	0.415	0.059	(A) (A)	
NGC 3675	0.085 ± 0.012	16.5	30.0	0.300	0.08	(B) (A)	
NGC 3681	0.199 ± 0.011	7.5	15.0	0.401	0.144	(B) (X)	
NGC 3686	0.253 ± 0.018	10.5	18.0	0.316	0.091	(B) (B)	
NGC 3726	0.213 ± 0.024	25.5	30.0	0.219	0.079	(B) (X)	
NGC 3887	0.207 ± 0.017	31.5	40.5	0.263	0.097	(B) (B)	
NGC 4027	0.623 ± 0.008	3.3	20.0	0.495	0.183	(B) (B)	
NGC 4051	0.280 ± 0.008	55.5	45.0	0.655	0.173	(B) (X)	
NGC 4123	0.428 ± 0.070	37.5	52.5	0.573	0.251	(B) (B)	
NGC 4136	0.131 ± 0.003	10.5	15.0	0.249	0.037	(B) (X)	
NGC 4145	0.356 ± 0.002	4.5	19.5	0.267	0.087	(B) (X)	
NGC 4151	0.119 ± 0.012	67.5	97.5	0.746	0.329	(B) (X)	
NGC 4293	0.355 ± 0.003	49.5	67.5	0.668	0.271	(B) (B)	
NGC 4303	0.259 ± 0.044	40.5	30.0	0.443	0.145	(B) (X)	
NGC 4314	0.442 ± 0.024	52.5	75.0	0.896	0.571	(B) (B)	
NGC 4394	0.272 ± 0.006	31.5	45.0	0.577	0.311	(B) (B)	
NGC 4450	0.131 ± 0.011	37.5	30.0	0.322	0.125	(B) (X)	

Table 3 – *continued*

Galaxy	Q_g	r_{Q_g} (arcsec)	Bar length (arcsec)	A_2	A_4	EFP/RC3	
NGC 4457	0.089 ± 0.004	31.5	45.0	0.435	0.095	(B) (X)	
NGC 4487	0.177 ± 0.035	10.0	22.2	0.176	0.071	(B) (X)	
NGC 4490	0.334 ± 0.032	7.5	18.0	0.188	0.041	(B) (B)	
NGC 4496	0.365 ± 0.004	7.5	25.5	0.283	0.055	(B) (B)	
NGC 4527	0.198 ± 0.026	46.5	82.5	0.600	0.200	(X) (X)	
NGC 4548	0.344 ± 0.017	55.5	67.5	0.723	0.338	(B) (B)	
NGC 4579	0.197 ± 0.020	34.5	45.0	0.494	0.246	(B) (X)	
NGC 4593	0.309 ± 0.020	45.5	61.0	0.765	0.367	(B) (B)	
NGC 4618	0.392 ± 0.046	10.5	33.0	0.327	0.105	(B) (B)	
NGC 4643	0.251 ± 0.004	43.5	67.5	0.828	0.516	(B) (B)	
NGC 4647	0.117 ± 0.010	10.5	11.5	0.310	0.115	(B) (X)	
NGC 4651	0.120 ± 0.046	16.5	22.5	0.207	0.044	(X) (A)	
NGC 4654	0.171 ± 0.005	7.5	19.5	0.175	0.063	(B) (X)	
NGC 4665	0.257 ± 0.023	37.5	60.0	0.615	0.306	(B) (B)	
NGC 4691	0.504 ± 0.027	13.5	45.0	0.803	0.419	(B) (B)	
NGC 4699	0.144 ± 0.027	10.0	14.4	0.382	0.086	(B) (X)	
NGC 4781	0.352 ± 0.061	16.7	38.8	0.323	0.131	(B) (B)	
NGC 4900	0.384 ± 0.041	7.5	18.0	0.369	0.103	(B) (B)	
NGC 4902	0.277 ± 0.026	16.7	22.2	0.526	0.277	(B) (B)	
NGC 4930	0.207 ± 0.022	34.4	44.4	0.607	0.313	(B) (B)	
NGC 4939	0.128 ± 0.052	15.1	17.4	0.284	0.109	(X) (A)	
NGC 4995	0.278 ± 0.047	22.5	22.5	0.377	0.124	(B) (X)	
NGC 5005	0.152 ± 0.000	28.5	45.0	0.362	0.122	(B) (X)	
NGC 5101	0.187 ± 0.015	45.2	69.6	0.708	0.386	(B) (B)	
NGC 5334	0.364 ± 0.010	10.5	18.0	0.285	0.108	(B) (B)	
NGC 5483	0.174 ± 0.003	7.8	13.3	0.210	0.090	(B) (A)	
NGC 5643	0.415 ± 0.013	33.6	46.4	0.433	0.257	(B) (X)	
NGC 5701	0.143 ± 0.000	30.0	49.9	0.466	0.196	(B) (B)	
NGC 5713	0.357 ± 0.033	10.5	30.0	0.600	0.210	(B) (X)	
NGC 5850	0.318 ± 0.010	61.5	90.0	0.693	0.366	(B) (B)	+ minibar
NGC 5921	0.416 ± 0.023	46.5	52.5	0.704	0.361	(B) (B)	
NGC 5962	0.148 ± 0.052	13.5	15.0	0.249	0.096	(B) (A)	
NGC 6221	0.436 ± 0.112	27.8	40.6	0.617	0.277	(B) (B)	
NGC 6300	0.187 ± 0.002	33.6	46.4	0.414	0.163	(B) (B)	
NGC 6384	0.136 ± 0.020	16.5	33.0	0.352	0.069	(B) (X)	
NGC 6782	0.165 ± 0.008	24.4	46.4	0.631	0.278	(B) (X)	
NGC 6902	0.075 ± 0.004	13.9	17.4	0.140	0.04	(B) (A)	
NGC 7418	0.192 ± 0.029	15.1	15.1	0.273	0.076	(B) (X)	
NGC 7479	0.696 ± 0.060	43.5	60.0	0.867	0.555	(B) (B)	
NGC 7552	0.395 ± 0.044	45.2	69.6	1.148	0.724	(B) (B)	
NGC 7582	0.436 ± 0.069	56.8	92.8	0.932	0.551	(B) (B)	
NGC 7723	0.349 ± 0.030	16.5	24.0	0.386	0.184	(B) (B)	
NGC 7727	0.096 ± 0.024	10.5	27.0	18.00	7.70	(Spec) (X)	
NGC 7741	0.687 ± 0.006	10.5	52.5	0.602	0.283	(B) (B)	
2MASS:							
NGC 1068	0.165 ± 0.010	11.0	15.0	0.391	0.149	(A)	
NGC 1097	0.279 ± 0.048	75.0	100.0	0.821	0.421	(B)	+ minbar
NGC 1232	0.210 ± 0.002	7.0	12.0	0.295	0.066	(X)	
NGC 1398	0.202 ± 0.011	39.0	55.0	0.406	0.275	(B)	
NGC 3521	0.096 ± 0.019	25.0	28.0	0.368	0.269	(X)	
NGC 4321	0.183 ± 0.027	61.0	90.0	0.335	0.230	(X)	+ minbar
NGC 4569(R)	0.175 ± 0.064	10.0	30.0	0.434	0.188	(X)	
NGC 4736	0.048 ± 0.004	11.0	15.0	0.156	0.070	(A)	
NGC 7513	0.483 ± 0.031	27.0	55.0	0.649	0.354	(B)	

Q_g measurements were repeated for all the galaxies in the sample by varying one parameter at a time. We also evaluate how important the bulge correction is, both statistically and for some individual galaxies.

The effect of orientation parameters was tested by repeating the measurement twice: by adding $\Delta q = 0.025$ to axial ratios in one run and by subtracting the same value in another run. Similarly, two set of runs were made by using $\Delta\phi = \pm 5^\circ$ (the range of

Table 4. Galaxies without Fourier bars.

Galaxy	Q_g	r_{Q_g} (arcsec)	EFP/RC3
OSUBGS			
ESO 138	0.148 ± 0.001	80.0	(A) (A)
NGC 157	0.326 ± 0.174	31.5	(A) (X)
NGC 278	0.063 ± 0.021	28.5	(A) (X)
NGC 488	0.032 ± 0.003	19.5	(A) (A)
NGC 908	0.183 ± 0.005	75.4	(A) (A)
NGC 1042	0.533 ± 0.209	31.5	(X) (X)
NGC 1058	0.138 ± 0.001	22.5	(A) (A)
NGC 1084	0.212 ± 0.025	35.5	(A) (A)
NGC 1309	0.148 ± 0.060	15.1	(X) (A)
NGC 1371	0.113 ± 0.003	19.7	(X) (X)
NGC 1792	0.151 ± 0.092	36.0	(A) (A)
NGC 2090	0.114 ± 0.005	10.4	(A) (A)
NGC 2196	0.070 ± 0.005	7.8	(A) (A)
NGC 2775	0.050 ± 0.010	46.5	(A) (A)
NGC 3169	0.090 ± 0.005	16.5	(A) (A)
NGC 3223	0.038 ± 0.003	69.9	(A) (A)
NGC 3423	0.099 ± 0.075	67.7	(A) (A)
NGC 3596	0.157 ± 0.044	46.5	(X) (X)
NGC 3646	0.241 ± 0.025	64.5	(X)(RING)
NGC 3684	0.085 ± 0.020	10.5	(X) (A)
NGC 3810	0.128 ± 0.022	16.5	(X) (A)
NGC 3893	0.148 ± 0.001	19.5	(X) (X)
NGC 3938	0.070 ± 0.005	58.5	(A) (A)
NGC 3949	0.276 ± 0.084	25.5	(X) (A)
NGC 4030	0.060 ± 0.013	16.7	(A) (A)
NGC 4138	0.046 ± 0.007	7.5	(A) ()
NGC 4212	0.234 ± 0.051	28.5	(X) (A)
NGC 4242	0.237 ± 0.062	40.5	(B) (X)
NGC 4254	0.122 ± 0.029	22.5	(X) (A)
NGC 4414	0.149 ± 0.003	28.5	(A) (A)
NGC 4504	0.136 ± 0.019	25.5	(B) (A)
NGC 4571	0.067 ± 0.027	40.5	(A) (A)
NGC 4580	0.109 ± 0.012	13.5	(A) (X)
NGC 4689	0.068 ± 0.001	58.5	(A) (A)
NGC 4698	0.084 ± 0.040	64.5	(A) (A)
NGC 4772	0.042 ± 0.013	70.5	(B) (A)
NGC 4775	0.134 ± 0.013	7.5	(A) (A)
NGC 4941	0.056 ± 0.008	49.5	(X) (X)
NGC 5054	0.090 ± 0.023	80.0	(X) (A)
NGC 5085	0.152 ± 0.021	22.0	(X) (A)
NGC 5121	0.024 ± 0.007	27.8	(A) (A)
NGC 5247	0.329 ± 0.150	75.4	(A) (A)
NGC 5248	0.269 ± 0.064	76.5	(A) (X)
NGC 5427	0.231 ± 0.074	38.3	(A) (A)
NGC 5676	0.102 ± 0.014	16.5	(X) (A)
NGC 6215	0.239 ± 0.130	26.7	(X) (A)
NGC 6753	0.039 ± 0.009	12.8	(A) (A)
NGC 6907	0.329 ± 0.154	29.0	(B) (B)
NGC 7083	0.073 ± 0.001	26.7	(A) (A)
NGC 7205	0.060 ± 0.017	63.8	(X) (A)
NGC 7213	0.023 ± 0.002	100.9	(A) (A)
NGC 7217	0.036 ± 0.001	13.5	(A) (B)
NGC 7412	0.415 ± 0.183	52.2	(X) (B)
NGC 7713	0.099 ± 0.015	26.7	(A) (B)
2MASS			
NGC 772	0.066 ± 0.020	25.0	(A)
NGC 2655	0.128 ± 0.004	19.0	(X)
NGC 2841	0.071 ± 0.008	37.0	(A)
NGC 2985	0.056 ± 0.001	11.0	(A)
NGC 3031	0.091 ± 0.031	29.0	(A)
NGC 3077	0.119 ± 0.016	9.0	(IO)
NGC 3486(R)	0.108 ± 0.002	15.0	(X)
NGC 3718	0.106 ± 0.007	73.0	(B)
NGC 3898	0.047 ± 0.000	13.0	(A)
NGC 4501	0.072 ± 0.026	89.0	(A)
NGC 4753	0.106 ± 0.019	59.0	(IO)
NGC 5457	0.225 ± 0.001	73.0	(X)
NGC 6643	0.118 ± 0.006	17.0	(A)

Table 5. Number of SA, SAB and SB galaxies in different classifications.

	SA	SAB	SB
RC3	46	50	59
H (visual)	33	26	98
H (Fourier)	53		105

uncertainties corresponds to the mean of the absolute deviations in comparison with García-Gómez et al. 2004, found in Section 2). Denoting $\Delta(Q_g)_q = Q_g(q + 0.025) - Q_g(q - 0.025)$ and $\Delta\,(Q_g)_\phi = Q_g(\phi + 5^\circ) - Q_g(\phi - 5^\circ)$, we obtain

$$\langle|\Delta(Q_g)_q|\rangle = 0.016,$$

$$\langle|\Delta(Q_g)_\phi|\rangle = 0.030.$$

Similar uncertainties are obtained if just barred galaxies are considered. Note that these are very conservative upper limits for the actual uncertainties, because the expected errors for individual galaxies have opposite signs with equal probabilities, effectively cancelling each other in sample averages.

Another possible uncertainty in our method is the sufficiency of the adopted number of Fourier components used ($m_{\max} = 10$). To check for this, we repeated all our measurements using all even components up to $m_{\max} = 20$ [denoted by $(Q_g)_{20}$]. The resulting difference turned out to be completely insignificant:

$$\langle(Q_g)_{20}/Q_g\rangle = 1.009 \pm 0.06,$$

$$\langle|(Q_g)_{20} - Q_g|\rangle = 0.004.$$

In practice, a much larger uncertainty in Q_g is caused by the assumed vertical scaleheight, which might also have systematic errors. In order to assess this, we again repeated our measurements twice, using for each galaxy both the maximum and minimum h_z values implied by the variation of h_z/h_r among each morphological type found by de Grijs (1998): the maximum is $h_z/h_r = 1, 1/3, 1/5$ for morphological types $T \leqslant 1, 2 \leqslant T \leqslant 4, T \geqslant 5$, respectively, while the minimum is $h_z/h_r = 1/5, 1/7, 1/12$ (standard average values used were $h_z/h_r = 1/4, 1/5, 1/9$). In comparison to using the standard values of h_z, we obtain the mean ratios (and standard deviation of individual ratios):

$$\langle(Q_g)_{\min\, h_z}/Q_g\rangle = 1.08 \pm 0.04,$$

$$\langle(Q_g)_{\max\, h_z}/Q_g\rangle = 0.81 \pm 0.12.$$

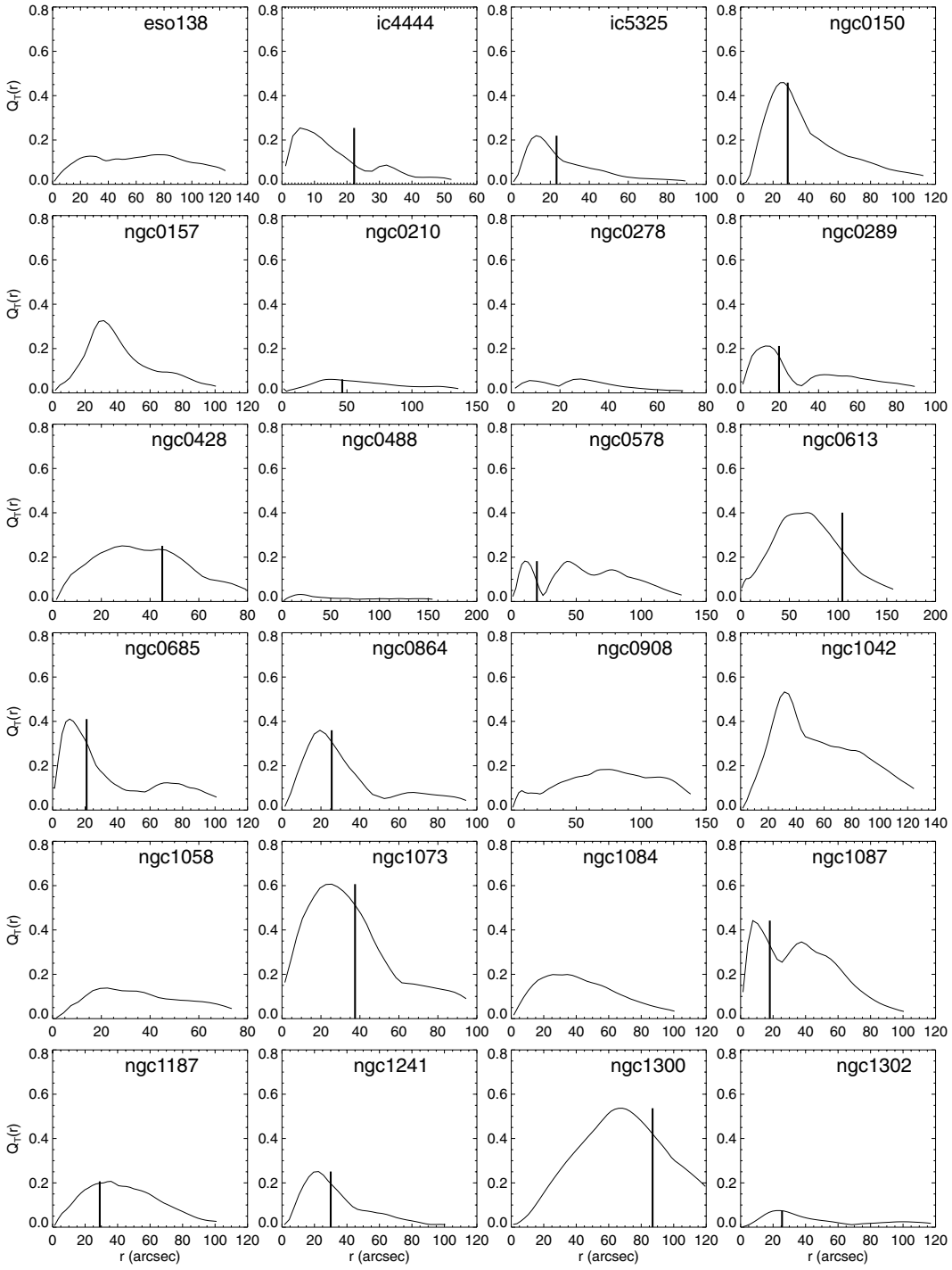

Figure 5. (Figs 5b–h can be found in the online version of this paper at http://www.blackwellpublishing.com/products/journals/suppmat/MNR/MNR8410/MNR8410sm.htm.) Radial profiles of the perturbation strength $Q_T(r) = |F_T(r, \phi)|_{max}/\langle|F_R(r, \phi)|\rangle$, where $|F_T(r, \phi)|_{max}$ is the maximum tangential force, and $\langle|F_R(r, \phi)|\rangle$ is the mean azimuthally averaged axisymmetric force at each radius. The vertical bar denotes the length of the bar, estimated from the phases of the $m = 2$ amplitude of density, assuming that it is maintained nearly constant in the bar region.

The relative uncertainty in Q_g increases toward earlier Hubble types, reflecting the larger range of uncertainty in the vertical scaleheight. This trend is depicted in Fig. 6: for example, for $T \leqslant 1$ the systematic use of the minimal h_z/h_r ratio yields Q_g values about twice as large in comparison to what the maximal h_z/h_r gives. Nevertheless, the trend of average Q_g increasing with T (BLS) is clearly not affected by this uncertainty. The estimation of the vertical scaleheight is particularly uncertain for galaxies with prominent outer rings (NGC 210, 1808 and 5701), because it is not clear whether the empirical relation between the vertical scaleheight and the radial scalelength of the disc is valid also for this type of galaxy.

The applied bulge correction is statistically not very important. For the barred galaxies in our sample we obtain

$$\langle Q_{g_{\text{no bulge}}}/Q_g\rangle = 1.07 \pm 0.32,$$

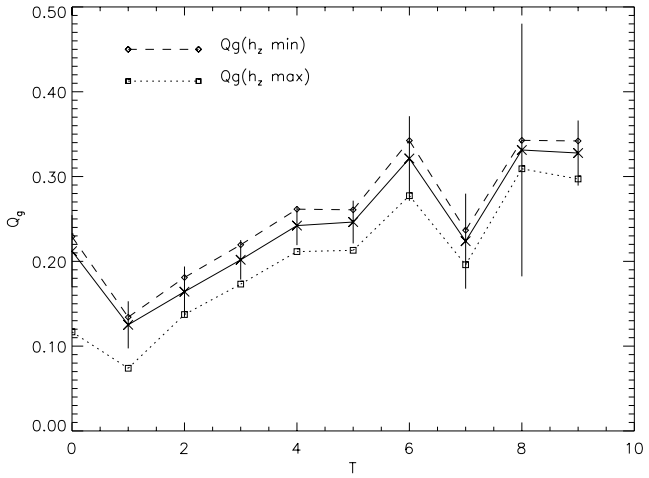

Figure 6. The maximal effect of the h_z/h_r uncertainty as a function of morphological type. The solid line shows the average value of $Q_{\rm g}$ obtained using the assumed standard h_z/h_r ratios (error bars correspond to the standard deviation of the mean), while the dashed (dotted) lines correspond to the mean values obtained when using systematically the minimum (maximum) ratio of h_z/h_r for each galaxy (see text for details).

where $Q_{\rm g\,no\,bulge}$ refers to values calculated with no special treatment of bulges, except that the $Q_{\rm T}$ maxima occurring conspicuously near the centre have been suppressed, by limiting the search of the maximum beyond five image pixels from the centre. This is a similar treatment as applied in LS and in Block et al. (2004); in the case when the bulge correction was applied, no such caution was needed. However, the influence of artificial bulge stretch can be large for some individual galaxies, especially if the bars/ovals reside inside a large bulge. Fig. 7 (left-hand panel) displays the difference in the Q_g values with and without correcting for the spherical bulge (but using the above defined five pixel limit), as a function of $r_{\rm bar}/r_{\rm eff}$. Clearly, for $r_{\rm bar}/r_{\rm eff}$ less than about 10, the bulge stretch starts to affect the measured force ratio. Note that the bulge stretch can either increase or decrease $Q_{\rm g}$ depending on whether the uncorrected bulge projects along or perpendicular to the bar in deprojection to face-on orientation. On the other hand, if no limitation were placed on the location of the $Q_{\rm T}$ maximum (Fig. 7, right-hand panel), a slight systematic increase in the case of no bulge correction starts to be evident ($\langle Q_{\rm g\,no\,bulge}/Q_{\rm g}\rangle = 1.16 \pm 0.45$), due to strong artificial force peaks sometimes produced near the centre. Altogether, although the effect of the bulge correction is minor, for example, when calculating the distribution of bar strengths (BLS), it enables us to better analyse the force profiles also in the bulge region. The correction assuming a spherical bulge light distribution and the case when the bulge light is not separated from the disc represent two extreme treatments of a bulge. The small difference in the obtained results suggests that, at least for statistical purposes, there is no obvious need for a more refined bulge correction. Any uncertainty in $Q_{\rm g}$, possibly originated using the Ferrers function for the bar model in the decomposition, is included in the estimated uncertainty due to the bulge.

6 BAR MORPHOLOGIES

As not all $Q_{\rm T}$ maxima are associated with bars, we have to specify what we mean by a bar. Our main criteria were that significant A_2 and A_4 amplitudes of density could be detected, and that their phases were maintained nearly constant in the bar region (the weakest detected bar in our sample has $A_2 = 0.12$). Another powerful tool to

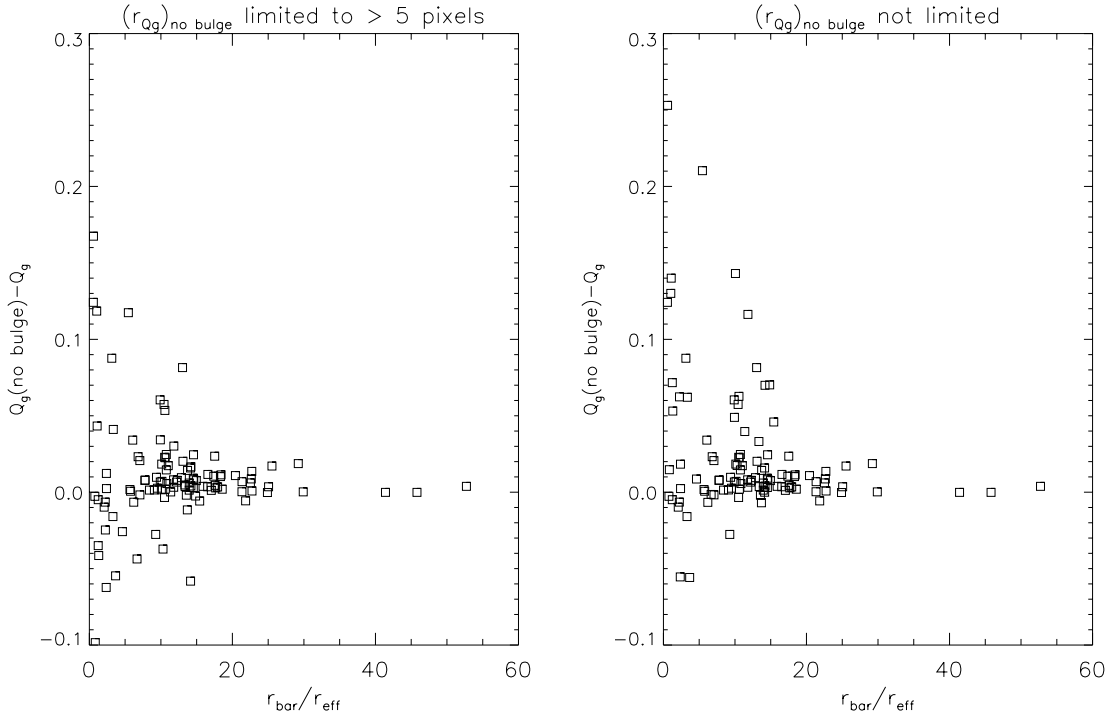

Figure 7. Effect of the applied spherical bulge correction for the barred galaxies of our sample. The difference between $Q_{\rm g}$ values in the case without and with the bulge correction is shown as a function of $r_{\rm bar}/r_{\rm eff}$, where $r_{\rm eff}$ is the effective radius of the bulge and $r_{\rm bar}$ is the bar length. On the left, the $Q_{\rm T}$ maxima occurring very near the centre have been suppressed for the non-corrected measurements, by limiting the search of maximum beyond five image pixels from the centre. On the right, no such limitation was placed, leading on average to somewhat larger excesses.

identify bars is to inspect the polar angle maps presented in logarithmic radial scale; bars generally have clear density condensations in their outer parts and the polar angle is not changed much in the radial direction. Also, in the presence of a bar, two well-defined maxima and two minima appear in the Q_T map in the form of a 'butterfly pattern'. The main limitation of these diagnostics is that no difference is made between a bar and an oval, which have to be distinguished by other means. Ovals are more round structures and generally also have lower surface brightnesses than bars.

In most cases, the above criteria unambiguously distinguished the bar, but some galaxies had to be inspected more carefully. There were seven galaxies (NGC 3646, 3810, 3949, 4212, 4242, 5054 and 5085) that were not classified as barred, although the $m = 2$ phases were maintained nearly constant at a certain radius of the disc. In NGC 3646, 3949, 3810 and 5054, the elongated structure appeared to be an oval, which was evident in the original images and also while looking at the 'butterfly patterns'. The 'butterfly patterns' of these galaxies showed structures where the angles between the locations of the Q_T peak and the bar/oval axis, α, were 55°, 42°, 59° and 45°, respectively. These types of large angles are typical for ovals. For NGC 4212, α is only 30°, but there is no $m = 4$ density amplitude typical for bars in the assumed bar region. For NGC 5085, the 'butterfly pattern' shows a typical spiral-like nature with four symmetrically distributed curved structures, which was the main reason why this galaxy was classified as non-barred. NGC 4242 looks like a peculiar galaxy with extremely diffuse structure, so that if there is a bar, it must also be diffuse. However, because of the lack of any clear sign of a bar it was classified as non-barred.

In RC3, bars are assumed to be strong when they belong to the de Vaucouleurs class B, and weak when they belong to AB-type systems. Similar classifications were made in the near-IR by EFP using the OSUBGS sample. In the optical, 71 per cent of the galaxies in our sample were found to have bars (B + AB), whereas in the near-IR the fraction of barred galaxies is 78 per cent. This means that a small fraction of bars in the optical are obscured by dust in the near-IR. However, the main difference between the classifications in the two wavelength regions is that in the near-IR bars belong to category B much more often than bars in the optical region (62 per cent versus 37 per cent of all galaxies). In principle, this can be an artefact, because there are only three bar bins: SA, SAB and SB. Bars probably look stronger to some extent in the near-IR, so that SAs can shift to SABs, and SABs can shift to SBs, but there is no extra bin for SBs to shift into. Thus, near-IR bars might pile up into the SB bin. The Fourier method picks up mainly the SB-type bars, which form 90 per cent of all barred galaxies as identified by Fourier methods. Also, except for four galaxies, NGC 4242, 4504, 4772 and 6907 (which has a minibar), all galaxies classified as SB by EFP are barred also according to our Fourier analysis. Additionally, among the barred galaxies there are also eight SAB-type systems and one SA galaxy as classified by EFP in the near-IR. It seems that some well-defined criterion is needed to judge whether a galaxy has a bar or not.

Does the above then mean that the Fourier method is capable of picking up only the strong bars? The amplitude limit of the $m = 2$ Fourier component for the weakest detectable bar in our sample is $A_2 = 0.12$, which is very similar to the lower limit of $A_2 = 0.09$ for the SAB-type galaxies. The weakest detected main bar in our sample has $Q_g = 0.06$, which is approximately the lower limit of the weakest bars in the classification by BB ($Q_g = 0.05$). This means that the Fourier method is capable of detecting both strong and weak bars. An interesting question is then why 68 per cent of the visually detected SAB-type galaxies in the near-IR turn out to be non-barred based on the Fourier method. In the following we discuss the morphological properties of some typical barred and non-barred galaxies in our sample.

6.1 Barred galaxies

NGC 4151 (Fig. 8a). This galaxy is classified as barred by EFP, and has an intermediate-type bar in RC3. According to all our indicators, this galaxy has a bar, but it seems not to be well developed: only two material condensations at the outer edges of the bar along the bar major axis are seen, giving it 'ansae'-type characteristics. This type of bar is rare in our sample, but is more typical for very early-type galaxies (see, for example, Buta 1995, 1996).

NGC 5701 (Fig. 8b, available in the online version). This is a galaxy with a bar and a well-defined outer pseudo-ring of type R'_2 (see appendix 3 of RC3 and Buta 1995). The ring is better defined in the *B*-band image. The bar itself appears inside an oval/lens feature. The bar has clear A_2 and A_4 amplitude peaks and their phases are maintained nearly constant in the bar region. Also, the 'butterfly pattern' forms four symmetric well-defined regions, as expected for a bar. The $m = 2$ amplitude peak in the polar angle map is very wide, which is the reason why the Q_T profile is also wide. In this case, no spiral arms are visible, so the wide amplitude and Q_T profiles seem to be characteristic for the bar itself.

The galaxies NGC 5101, 3275 and 3504 are all cases having a classical well-developed bar and an inner ring located at the distance of the outer edge of the bar. However, they also have other characteristics that make them unique compared with the other galaxies.

NGC 5101 (Fig. 8c, available in the online version; see also Fig. 2). This is another case of an 'ansae'-type bar with two strong material condensations at the outer edges. The galaxy has an inner ring filled by the bar along its major axis. This galaxy also has two amplitude maxima in the polar angle map, appearing along the bar major axis. The outer maximum is located at the radius of the inner ring, showing also short spiral-like arm segments, which might be relics of the ring formation. The A_2 profile for this galaxy is asymmetric, declining rather rapidly after the maximum, which is manifested also in the Q_T profile. A natural explanation for this decline is that the bar ends near to the inner ring. Like NGC 5701, NGC 5101 has an R'_2 outer pseudo-ring in blue light (appendix 3 of RC3).

NGC 3275 (Fig. 8d, available in the online version). This is also an example of a bar/ring system, but in this case there are also large-scale spiral arms outside the bar. The Q_T profiles in NGC 5101 and 3275 have different shapes. The broad hump in the Q_T profile of NGC 3275 is caused by the strong material condensations at the two ends of the bar coinciding with the radius of the inner ring. It is not clear in the direct image whether these blobs are part of the inner ring or part of the large-scale spiral arms.

NGC 3504 (Fig. 8e, available in the online version; see also Fig. 2). This is another example of a bar/ring system with prominent spiral arms, which are forming a ring. This is a good example of galaxies showing a bar with two blobs at the ends of the bar, manifesting also some spiral-like characteristics. The amplitude profile also has two peaks in the bar region. In this case, the tiny spiral arm segments are not related to the outer spiral arm structure, being rather part of the bar/inner ring system. The Q_T profile is asymmetric, but in the opposite direction than in NGC 5101. The outer pseudo-ring of NGC 3504 is type R'_1 (appendix 3 of RC3).

NGC 4548 (Fig. 8f, available in the online version). This is a galaxy with a bar and spiral arms, but no inner ring attached at the

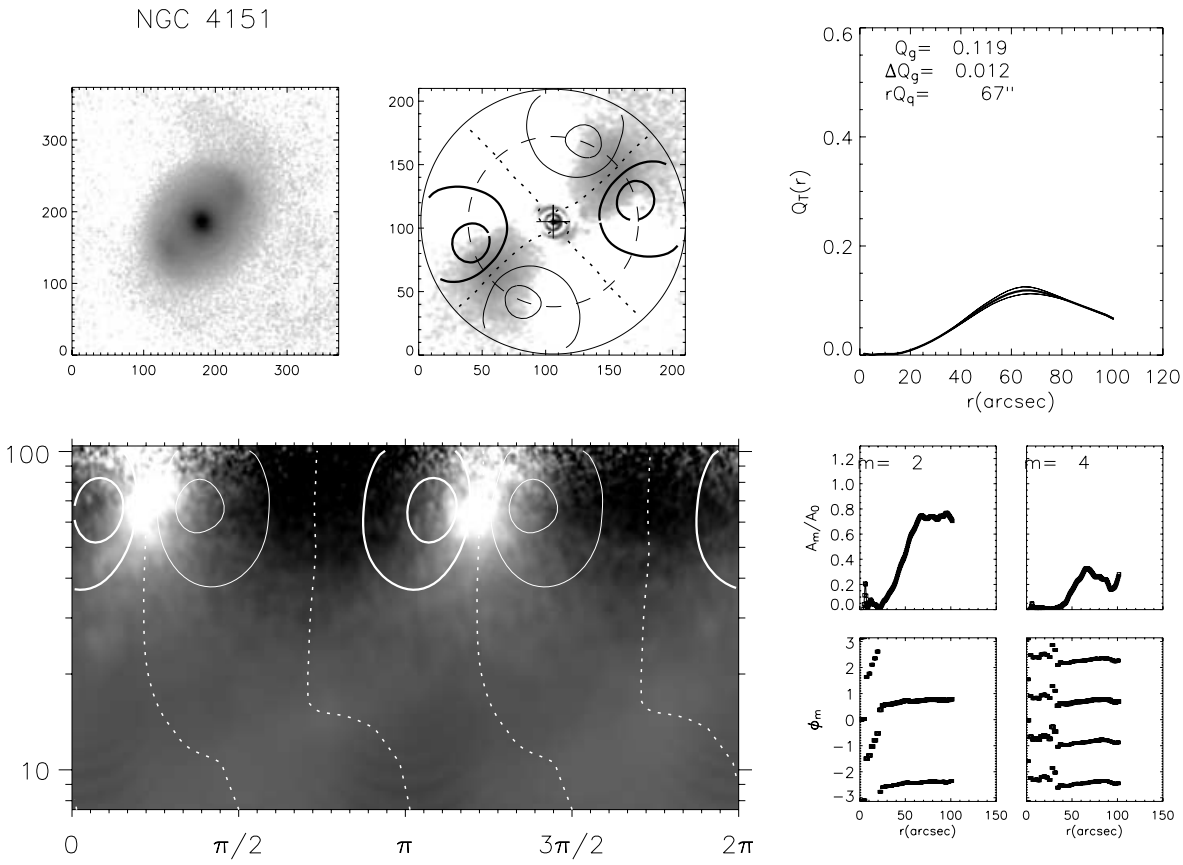

Figure 8. (Figs 8b–j can be found in the online version of this journal at http://www.blackwellpublishing.com/products/journals/suppmat/MNR/MNR8410/MNR8410sm.htm.) For some example galaxies, results are shown of the Fourier method used to calculate the perturbation strengths. In the upper-left corner is shown the original galaxy image in the *H* band, and in the middle upper panel the image where the $m = 0$ component is subtracted. Overlaid on the image is the 'butterfly pattern', which shows the regions of the maximum relative tangential forces in contours divided into intervals of 0.1 bar strength units. The dotted lines indicate the regions where the tangential forces change the sign. In the upper-right corner are shown the radial Q_T profiles calculated in the four image quadrants (thin lines) and the average profile is indicated by a thick line. The lower left-hand panel is the butterfly plot in log-polar coordinates: the contours and dotted lines are the same as in the upper middle panel. In the right lower corner are shown the $m = 2$ and $m = 4$ Fourier amplitudes and phases. In all figures the radial distances are in arcsec.

radius of the bar. The spiral arms start as arc-like structures at the two ends of the bar and continue to form global spiral patterns. It seems that the formation of the inner ring is not yet completed. In this case, the A_2 amplitude profile is affected by the partial superposition of the global spiral arms. This type of bar/spiral structure is quite typical in the OSUBGS sample, being found also in NGC 150, 289, 864, 1832, 2566, 3261, 2548, 4579, 5493 and 4781. For this type of galaxy, it would be valuable to apply the bar/spiral separation method (Buta et al. 2003).

The two barred galaxies, NGC 7552 and 7479, are examples of systems having a bar and prominent two-armed spirals.

NGC 7552 (Fig. 8g, available in the online version; see also Fig. 2). This is a peculiar case of a bar and two spiral arms forming an outer pseudo-ring (type R'_1; Buta 1995). One of the spiral arms, starting from the end of the bar, is more prominent than the other arm, which seems to have no clear continuation with the bar. The bar itself is very dusty and shows a lot of structure. The polar angle map shows how the spiral arm attached to the bar is superimposed with the bar. While looking at the original image, this galaxy has similarities with NGC 3504: in both cases, there are blobs at the two ends of the bar showing some characteristics of spiral arms. Also, as in NGC 3504, the small spiral arm segments are not a continuation of the global spiral patterns. The main difference, compared with NGC 3504, is that NGC 7552 has no inner ring.

NGC 7479 (Fig. 8h, available in the online version). This is a late-type galaxy having a bar and two strong spiral arms starting from the two ends of the bar. In this case, two spiral arms form a global pattern in the disc. The arms are also forming a ring at the radius of the bar major axis. The A_2 density maximum is probably a combination of both bar and spiral arms.

6.2 Non-barred SAB-type galaxies

The two galaxies NGC 1371 and 5054 are chosen to illustrate typical SAB-type galaxies as defined by EFP in the near-IR. Some of the SAB-type bars in the IR might also be spiral arms, which look like a bar in projection. Such an example is NGC 4504, which is classified as non-barred in RC3.

NGC 1371 (Fig. 8i, available in the online version; see also Fig. 2). This is classified as SAB both in RC3 and by EFP in the near-IR. It has a peak in the Q_T profile, typical for barred galaxies, but our main bar indicators do not show a bar: the $m = 2$ phase is not maintained constant in the assumed bar region, and the 'butterfly pattern' shows a spiral-like nature. Also, in the direct image the

structure in the region of the Q_T peak shows a spiral-like nature. However, while looking at the polar angle map it is interesting to note that this galaxy has blobs at $r = 20$ arcsec, which coincide with the peak in the Q_T profile. Therefore, it is possible that this galaxy has a curved weak bar. Other similar cases in our sample are NGC 1042 and possibly also NGC 3596.

NGC 5054 (Fig. 8j, available in the online version). Another more typical group of SAB-type galaxies are those clearly having no bar, the non-axisymmetric forces being rather induced by ovals. Such galaxies are, for example, NGC 3893, 4254, 5054, 5085, 6215, 7205 and 7412, of which NGC 5054 is shown as an example. The oval is seen at $r < 20$ arcsec having nearly constant $m = 2$ phase in the oval region and a bar-like 'butterfly pattern'. The oval can be distinguished from a bar by its small major-to-minor axial ratio, and also by the relatively large angle between the two amplitude maxima in the butterfly pattern ($\alpha = 45^\circ$). The tangential forces induced by the oval are relatively weak for this galaxy, which is generally the case also for the other galaxies with ovals in our sample.

7 SUMMARY

We have calculated perturbation strengths for a well-defined magnitude-limited sample of 180 galaxies, based on 158 galaxies from the OSUBGS and 22 galaxies from the 2MASS. We use a gravitational bar torque method, in which the ratio of the tangential force to the azimuthally averaged mean axisymmetric radial force is used as a measure of the perturbation strength. The gravitational potential is inferred from a 2D H-band light distribution using a polar method, assuming that the light traces the mass and that the M/L ratio is constant throughout the disc. The data presented here have been previously used to derive the distribution of bar strengths for spiral galaxies (BLS) and to compare bar strengths in active and non-active galaxies (LSB).

Special attention has been given to correcting the deprojected images for artificial stretching of the bulge light. For this purpose, the orientation parameters of the discs were measured from the relatively deep B-band images by fitting ellipses to the outer isophotes. We found that, for some of the galaxies, the orientation parameters given in RC3 deviated significantly from our values. However, the correlation between our measurements and those by García-Gómez et al. (2004) was quite good. Artificial stretching of the bulges was avoided by separating the mass of the bulge from that of the disc. The bulge mass was then added back after deprojecting the disc to face-on orientation by assuming that the mass of the bulge is spherically distributed. This correction is important for the estimation of bar strengths for galaxies in which the bars appear inside large bulges.

We used a three-component 2D decomposition method where the discs were modelled by an exponential function, the bulges by the generalized Sérsic (1968) function, and the bar by a Ferrers function. To our knowledge, this is the first time that a three-component 2D method has been applied to a large sample of galaxies. We have found that fitting the bar model in the decomposition is important: if a bar is not taken into account in the decomposition, the flux of the bulge and the B/D ratio are easily overestimated. Also, if the bar is large, omission of the bar model might even underestimate the scalelength of the disc.

We have shown the importance of using some well-defined criteria while identifying bars in galaxies. A Fourier method is used, requiring that the phases of the density amplitudes of the main modes of bars, $m = 2$ and $m = 4$, are maintained nearly constant in the bar region. This method largely selects SB-type galaxies (as classified in the near-IR), which form 90 per cent of the barred galaxies in our sample. Additionally, 32 per cent of the SAB-type systems were found to be barred. The advantage of our method is that it is also capable of identifying weak bars, which in the ellipticity profiles might be overshadowed by the luminous discs.

The most remarkable result of this study is that even 68 per cent of the SAB galaxies, as classified in the near-IR, most probably are not barred galaxies at all. They are typically systems having a central oval and, in some cases, manifesting strong two-armed or multi-armed spiral arms, which all are capable of inducing tangential forces at some level. The perturbation strengths induced by ovals are relatively weak, being peaked at $Q_g = 0.15$, whereas the tangential forces induced by spiral arms can be either very weak (multi-armed spirals) or strong (two-armed spirals) amounting up to $Q_g = 0.6$. However, compared to bar-induced perturbations, similar tangential forces induced by spirals are effectively weaker in the central parts of the galaxies, because the force maxima appear at larger distances from the galaxy centres. As noticed by LSB, the distributions of Q_g and r_{Q_g} for SA- and SAB-type galaxies are remarkably similar, except for the innermost bins (see their fig. 9), thus indicating a similar origin of the tangential forces. In fact, 30 per cent of the SA-type galaxies in our sample have ovals inducing similar perturbation strengths, as found for many SAB-type systems. This is consistent with the picture outlined by Kormendy (2004), where ovals in all de Vaucouleurs family classes might play some role for the origin of the non-axisymmetric forces in galaxies.

In addition to these typical cases, there are also galaxies among SAB-type systems that might have weak non-classical bars. These bars have a spiral-like nature (see, for example, Jogee et al. 2002), and might form in weakly centrally concentrated discs. However, more thorough investigation is needed to verify their true nature.

ACKNOWLEDGMENTS

This paper makes use of data products from the 2MASS, which is a joint project of the University of Massachusetts and the Infrared Processing and Analysis Center/California Institute of Technology, funded by the National Aeronautics and Space Administration (NASA) and the National Science Foundation (NSF). It also uses the NASA/IPAC Extragalactic Database (NED), operated by the Jet Propulsion Laboratory in Caltech. EL and HS acknowledge the Magnus Ehrnrooth Foundation and the Academy of Finland for significant financial support. RB and SV acknowledge the support of NSF Grant AST-0205143 to the University of Alabama. We also acknowledge Paul Eskridge for many useful discussions.

REFERENCES

Block D., Buta R., Knapen J., Elmegreen D., Elmegreen B., Puerari I., 2004, AJ, 128, 183
Buta R., 1995, ApJS, 96, 39
Buta R., 1996, in Buta R., Crocker D. A., Elmegreen B. G., eds, ASP Conf. Ser. Vol. 91, Barred Galaxies. Astron. Soc. Pac., San Francisco, p. 11
Buta R., Block D., 2001, AJ, 550, 243 (BB)
Buta R., Block D., Knapen D., 2003, AJ, 126, 1148
Buta R., Laurikainen E., Salo H., 2004, AJ, 127, 279 (BLS)
Byun Y. I., Freeman K. C., 1995, ApJ, 448, 563
Combes F., Sanders R., 1981, A&A, 96, 164
Crocker D., Baugus P., Buta R., 1996, ApJS, 105
de Grijs R., 1998, MNRAS, 299, 595
de Jong R., 1996, A&A, 313, 45
de Souza R., Gadotti R., dos Anjos S., 2004, ApJS, 153, 411
de Vaucouleurs G., Freeman K. C., 1972, Vistas Astron., 14, 163

de Vaucouleurs G., de Vaucouleurs A., Corwin H. G., Jr, Buta R., Paturel G., Fouque P., 1991, Third Reference Cataloque of Bright Galaxies. Springer-Verlag, New York (RC3)
Eskridge P. B. et al., 2002, ApJS, 143, 73 (EFP)
García-Gómez C., Barberá C., Athanassoula E., Bosma A., Whyte L., 2004, A&A, 421, 595
Jogee S., Knapen J. H., Laine S., Shlosman I., Scoville N. Z., Englmaier P., 2002, ApJ, 570, L55
Knapen J. H., de Jong R. S., Stedman S., Bramich D. M., 2003, MNRAS, 344, 527
Kormendy J., 2004, in Block D. L., Freeman K. C., Puerari I., Groess R., Block E. K., eds, Penetrating Bars Through Masks of Cosmic Dust: The Hubble Tuning Fork Strikes a New Note. Kluwer, Dordrecht, in press
Laurikainen E., Salo H., 2000, A&A, 141, 103
Laurikainen E., Salo H., 2002, MNRAS, 337, 1118 (LS)
Laurikainen E., Salo H., Buta R., 2004, ApJ, 697, 103 (LSB)
MacArthur A. A., Courteau S., Holtzman J., 2003, ApJ, 582, 689
Möllenhoff C., Heidt J., 2001, A&A, 368, 16 (MH)
Peng C. Y., 2002, AJ, 124, 294
Peng C. Y., Ho L., Impey C. D., Rix H., 2002, AJ, 124, 266
Quillen A., Frogel J., Gonzalez R., 1994, ApJ, 437, 162
Salo H., Rautiainen P., Buta R., Purcell G. B., Cobb M. L., Crocker D. A., Laurikainen E., 1999, AJ, 117, 792
Sanders R., Tubbs A., 1980, ApJ, 235, 803
Sérsic J. L., 1968, Atlas de Galaxias Australes. Observatorio Astronomico, Cordoba
Shaw M. A., Gilmore G., 1989, MNRAS, 237, 903
Simard L. et al., 2002, ApJS, 142, 1
Skrutskie M. F. et al., 1997, in Garzon F. et al., eds, The Impact of Large-Scale Near-IR Surveys. Kluwer, Dordrecht, p. 25
Tully B., 1988, Nearby Galaxies Catalogue. Cambridge Univ. Press, Cambridge
Wadadekar Y., Robbason B., Kembavi A., 1999, AJ, 117, 1219

This paper has been typeset from a TEX/LATEX file prepared by the author.